

Enhancing GNSS Water Vapour Retrieval via Synergistic Microwave Radiometry: Thermodynamic Error Diagnosis and Bias Correction

Avinash N. Parde¹, Christina Oikonomou¹, Haris Haralambous^{1,2}

¹Frederick Research Center, Nicosia, 1036, Cyprus

²Frederick University, Nicosia, 1036, Cyprus

Correspondence: Avinash N. Parde (res.pav@frederick.ac.cy)

Abstract.

The retrieval of Precipitable Water Vapour (PWV) from Global Navigation Satellite Systems (GNSS) in thermodynamically complex environments is significantly limited by the accuracy of the weighted mean temperature (T_m). This study evaluates the efficacy of static climatological models versus dynamic ground-based microwave radiometry for T_m determination in the Eastern Mediterranean, a region characterized by sharp refractivity gradients. Using the Cyprus GNSS Meteorology Enhancement research project (CYGMEN) infrastructure in Nicosia, the performance of the ERA5-based HGPT2 model and a co-located Microwave Radiometer (MWR) was assessed against radiosonde (RS) profiles during the 2025 warm season (Spring–Summer). Diagnostic analysis reveals that the static HGPT2 model fails to resolve the diurnal thermodynamic decoupling between the boundary layer and the free troposphere, leading to a systematic overestimation of T_m exceeding 6 K during peak solar insolation. Conversely, the MWR captures short-term thermodynamic variability ($r=0.98$) but exhibits a systematic cold bias of -1.91 K in raw retrievals. It is demonstrated that a site-specific linear bias correction reduces the MWR T_m Root Mean Square Error (RMSE) from 2.32 K to 1.43 K, significantly outperforming the empirical model. Sensitivity analysis confirms that thermodynamic uncertainty dominates the error budget, outweighing uncertainties in refractivity constants by an order of magnitude. Consequently, standard climatological retrievals diverge from the synergistic MWR-GNSS method during extreme hygrometric events, introducing systematic PWV biases exceeding 1.0 mm when moisture levels surpass 45 mm. The synergistic coupling of real-time radiometric T_m with GNSS data is therefore meaningful for generating climate-quality PWV records in semi-arid coastal regions.

1 Introduction

Atmospheric water vapour (WV) is the primary greenhouse gas, contributing approximately 60 % to the natural greenhouse effect and playing a vital role in regulating the Earth's thermodynamic budget (Kiehl and Trenberth, 1997; Trenberth et al., 2005). Furthermore, WV is the main driver of latent heat transport, influencing convective systems and global precipitation patterns. High-frequency variations in Precipitable Water Vapour (PWV) correlate strongly with atmospheric instability and are a key factor in the initiation of severe weather. Specifically, rapid temporal gradients in PWV often precede heavy rainfall

32 and flash floods, acting as a reliable precursor for convective storms (Brenot et al., 2013). Consequently, assimilating high-
33 resolution PWV data into Numerical Weather Prediction (NWP) models significantly improves short-range precipitation "now-
34 casting" (Bennitt and Jupp, 2012). Accurate PWV retrieval is especially crucial for the Eastern Mediterranean, a climate change
35 "hotspot" warming faster than the global average (Giorgi, 2006; Lelieveld et al., 2012). This region is characterized by complex
36 topography and land-sea contrasts, which create sharp atmospheric refractivity gradients. The Eastern Mediterranean faces a
37 hydro-climatic paradox: a long-term drying trend (-0.5 mm/decade) alongside increasing high-intensity, short-duration flash
38 flood events (Zittis et al., 2019; Ziv et al., 2021). GNSS-derived PWV in this region exhibits strong diurnal cycles with
39 amplitudes up to 5 mm, which are closely correlated with atmospheric instability (Ziskin Ziv et al., 2020). Despite this
40 vulnerability, the Eastern Mediterranean currently lacks dense, continuous atmospheric profiling networks. Traditional
41 observation methods, such as radiosondes (RS), fail to resolve these mesoscale events due to low temporal resolution (typically
42 12-hour intervals) and significant spatial gaps (Soden and Lanzante, 1996). While satellite-based passive remote sensing offers
43 global coverage, it is often limited by revisit times, daylight dependence, or data degradation in coastal zones due to land
44 contamination in the microwave footprint (Bennartz and Bauer, 2003).

45 These limitations underscore the necessity for ground-based remote sensing techniques that offer continuous, all-weather
46 operability. Ground-based Global Navigation Satellite Systems (GNSS) meteorology has emerged as a robust technique for
47 atmospheric sounding since the seminal proposal by Bevis et al. (1992). By estimating the Zenith Total Delay (ZTD) of GNSS
48 signals traversing the neutral atmosphere, the Zenith Wet Delay (ZWD) can be isolated by subtracting the Zenith Hydrostatic
49 Delay (ZHD), which is accurately modeled from surface pressure observations (Saastamoinen, 1972). GNSS-derived PWV
50 offers significant advantages, including high temporal resolution (sub-hourly), all-weather availability, and cost-efficiency by
51 leveraging existing geodetic infrastructure (Guerova et al., 2016; Jones et al., 2020).

52 The retrieval of PWV from GNSS ZWD relies on a dimensionless conversion factor, Π , which is a function of the
53 atmospheric weighted mean temperature, T_m . Defined physically as $\int(e/T)dz/\int(e/T^2)dz$ (Askne and Nordius, 1987), T_m
54 encapsulates the thermal state of the atmospheric column. Because the conversion factor (Π) is nearly linearly proportional to
55 T_m , any relative error in the T_m estimation strictly propagates as an equivalent relative error in the final PWV retrieval. During
56 severe moisture events with an PWV of 50 mm, this translates to an absolute error of ~ 0.18 mm. Consequently, a 1 % relative
57 error in T_m translates strictly to a 1 % relative error in PWV. Therefore, alongside the substantial errors inherent in ZTD
58 estimation—such as mapping function inaccuracies and surface pressure interpolation for the ZHD (Ning et al., 2016)—the
59 determination of T_m remains one of the primary sources of uncertainty in GNSS meteorology. In the absence of in-situ profiles,
60 T_m is commonly estimated using empirical regression models or global climatological models. However, earlier studies have
61 demonstrated that empirical T_m regressions, such as the Bevis model (Bevis et al., 1992), introduce relative PWV errors of 1–
62 2 % due to weak T_s – T_m correlations in coastal and equatorial regions, where annual/semiannual variations are not adequately
63 captured (Yao et al., 2014; Lan et al., 2016). Similarly, global grid-based T_m models like GPT2w achieve RMSE < 4 K at ~ 80

64 % of mid-latitude sites but degrade in data-sparse areas like the Middle East and Africa, where reanalysis quality is limited
65 (Böhm et al., 2015; Jiang et al., 2019). The Hourly Global Pressure and Temperature 2 (HGPT2) model represents a major
66 advancement by providing hourly estimates derived from ERA5 reanalysis (Mateus et al., 2021). Despite recent validation of
67 GPT2w and ECMWF models for Precipitable Water Vapour (PWV) retrieval in the Mediterranean (Oikonomou et al. 2018),
68 a critical gap exists: the quantification of vertical interpolation errors in these models, especially over complex coastal terrains.
69 For instance, while recent validation studies in Cyprus demonstrate strong GNSS-PWV correlations (>0.6) with ERA5 during
70 extreme precipitation, persistent reanalysis interpolation errors are highlighted in mountainous areas (Giannadaki et al., 2025).
71 This lack of validation for HGPT2's performance in the complex topography of the Eastern Mediterranean potentially
72 exacerbates PWV biases during extreme events.

73 An alternative approach to deriving T_m is the use of ground-based Microwave Radiometers (MWR). MWRs measure
74 brightness temperatures at multiple frequencies to retrieve continuous vertical profiles of temperature and humidity. Ground-
75 based MWRs have been shown to retrieve T_m with RMSE $\sim 1\text{--}2$ K in mid-latitudes, outperforming empirical models during
76 synoptic anomalies (Cimini et al., 2010; Crewell and Löhnert, 2007; Löhnert et al., 2012). While multi-site intercomparisons
77 reveal that MWR retrievals can exhibit upper-tropospheric cold biases (up to 5 K at >2 km altitude) (Van Malderen et al.,
78 2014; Steinke et al., 2015), simple linear corrections can reduce RMSE by 20–40 % (Ning and Elgered, 2021). Operational
79 GNSS–MWR synergies for T_m bias correction have documented gains in PWV accuracy (10–30 % RMSE reduction) in
80 European networks (Vaquero-Martínez et al., 2018; Li et al., 2020). However, such applications are rare in the semi-arid
81 Eastern Mediterranean, where MWR could critically mitigate reanalysis uncertainties.

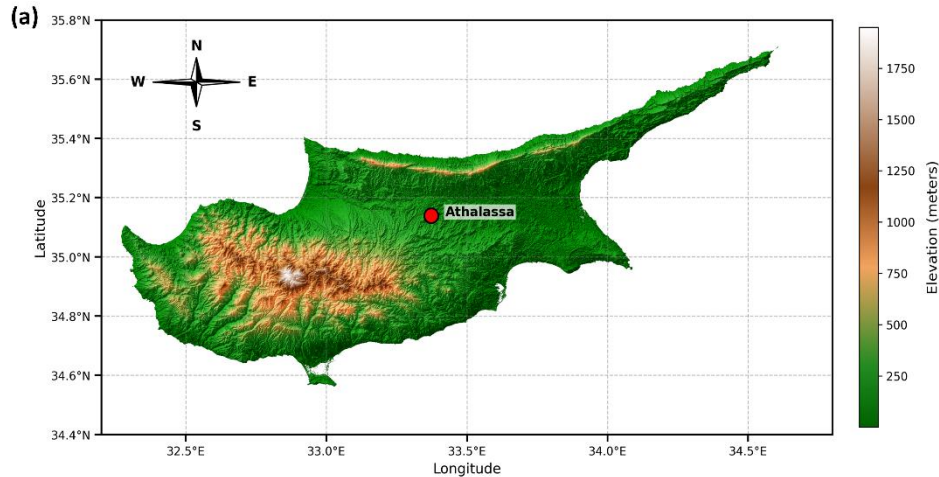
82 This study leverages the infrastructure of the CYGMEN (Cyprus GNSS Meteorology Enhancement) project, which is
83 establishing a dense, multi-sensor meteorological network in Cyprus. The network, termed CyMETEO, integrates a dense
84 array of continuous GNSS stations distributed across the island. Due to the high cost and operational complexity of radiometric
85 profiling, the network currently features a single, centralized thermodynamic 'supersite' at the Athalassa observatory, where a
86 GNSS receiver is strictly co-located with a MWR and a RS launch facility. This unique instrumental setup provides an ideal
87 testbed for inter-comparing atmospheric retrieval techniques in a coastal, semi-arid environment. The primary objective of this
88 manuscript is to evaluate the accuracy of GNSS-derived PWV over the Eastern Mediterranean by assessing the performance
89 of different T_m determination strategies. We specifically investigate the efficacy of the HGPT2 model compared to MWR-
90 derived T_m and RS benchmarks. The study aims to quantify the error budget of GNSS-PWV and determine whether the
91 inclusion of MWR data provides statistically significant improvements over the state-of-the-art HGPT2 model. The manuscript
92 is organized as follows: Section 2 describes the study area and the instrumentation of the CyMETEO network; Section 3 details
93 the methodology for GNSS processing, ZTD estimation, and the mathematical derivation of T_m from different sources; Section
94 4 presents the validation results and statistical analysis against RS reference data; and Section 5 concludes with
95 recommendations for operational PWV monitoring strategies in the region.

96

97 **2 Data and Methodology**

98 **2.1 Observational Site and CYGMEN Infrastructure**

99 The observational campaign was conducted at the Athalassa atmospheric observatory in Nicosia, Cyprus (35.15°N, 33.40°E,
100 160 m a.s.l.), situated in the central Mesaoria plain. The site is characterized by complex topography, bounded by the Troodos
101 Mountain to the southwest and the Pentadaktylos Mountain to the north, as shown in Fig. 1a. This study presents the first
102 comprehensive analysis of radiometric data acquired under the CYGMEN infrastructure project, established to monitor the
103 thermodynamic state of the Eastern Mediterranean atmosphere. To ensure robust thermodynamic profiling and validation,
104 three primary datasets were collated, as shown in Table 1:



(b)



(c)



(d)



105 **Figure 1.** Location and instrumentation at Athalassa, Cyprus. (a) Site location on the island's elevation map. (b) GNSS reference station.
106 (c) RPG-HATPRO radiometer. (d) Radiosonde balloon launching.
107

108

109 **Table 1:** Summary of Instrumentation and Datasets

Parameter	Microwave Radiometer (MWR)	Radiosonde (RS)	GNSS Station
Instrument Model	HATPRO-Gen5 (RPG)	Vaisala RS41-SGP	GNSS Receiver LEICA GR50 (Collocated)

Role in Study	Synergistic thermodynamic profiling (temperature and humidity) and PWV estimation	<i>In-situ</i> "Ground Truth" Reference	ZTD Source for PWV Retrieval
Observation Type	Passive remote sensing (22–58 GHz)	<i>In-situ</i> vertical profile (balloon-borne)	Continuous satellite signal delay
Key Variables	Brightness Temp (T_B), $T(z)$, $\rho_v(z)$, PWV	$P(z)$, $T(z)$, $RH(z)$, Geopotential Height	Zenith Total Delay (ZTD)
Vertical Range	Surface to 10 km (94 levels)	Surface to burst altitude (~30 km)	Column-integrated (single value)
Temporal Resolution	High frequency (~1 s raw, resampled to 15 min)	Periodic (launch dependent)	Continuous (high rate)
Accuracy / Noise	T_B noise < 0.11 K (K-band), < 0.32 K (V-band)	T : 0.3 K, RH : 4 % (Manufacturer spec)	ZTD precision ~mm level
Auxiliary Data	Vaisala WXT536 (Rain, Surface Met)	GPS position/height	Surface Pressure

110

111 2.2 Instrumentation and Data Processing

112 2.2.1 Microwave Radiometry (MWR)

113 The RPG-HATPRO radiometer observes downwelling atmospheric brightness temperatures (T_B) across 14 channels: seven in
114 the K-band (22–31 GHz) sensitive to water vapour, and seven in the V-band (51–58 GHz) sensitive to oxygen for temperature
115 profiling. This instrument enables the continuous retrieval of temperature (T) and absolute humidity (ρ_v) profiles on a
116 standardized grid of 94 vertical levels from the surface up to 10 km. The vertical resolution is optimized for the planetary
117 boundary layer (PBL), ranging from 10–30 m up to 500 m, and decreasing to 100–500 m in the free troposphere. For this
118 study, high-frequency MWR observations were resampled to 15-minute intervals to align with GNSS processing epochs. It is
119 a well-documented limitation of passive microwave radiometry that retrieval accuracy degrades significantly during
120 precipitation, as liquid water on the instrument's radome heavily contaminates the measured brightness temperatures (Foth et
121 al., 2024; Parde et al., 2025; Pakkattil et al., 2025; Ware et al., 2004). Because this study focused on the warm, dry season in
122 the Eastern Mediterranean (March–October 2025), rainfall events were naturally sparse. Nevertheless, to ensure data integrity,
123 real-time precipitation flags generated by the co-located Vaisala WXT536 surface weather transmitter were utilized as a strict
124 quality-control filter. Any MWR profiles retrieved during active precipitation events were excluded from the dataset to prevent
125 wet-radome anomalies from artificially skewing the thermodynamic bias analysis. To diagnose potential biases in the MWR-
126 derived T_m , the dataset was split into a training Set (April–June 2025) for regression modeling and a validation Set (July–
127 October 2025) for independent testing. In addition to thermodynamic profiling, the MWR's native retrieval algorithm possesses

128 the capacity to directly estimate PWV from its K-band brightness temperatures.

129 Any MWR profiles retrieved during active precipitation events were excluded from the dataset to prevent wet-radome
130 anomalies from artificially skewing the thermodynamic bias analysis. To mitigate T_m errors in MWR, a supervised linear
131 regression model was developed to calibrate the MWR observations. For robust independent validation, the collocated dataset
132 was separated into two distinct temporal subsets: the training Set (April – June 2025), which was used to derive the regression
133 coefficients, and the validation Set (July – October 2025), which was used exclusively to test the correction's performance on
134 unseen data. A simple linear correction model was fitted to the training data using Ordinary Least Squares (OLS) minimization.
135 The relationship is defined in Eq. (1) as:

$$136 \quad T_{m,corr} = \alpha \cdot T_{m,MWR} + \beta \quad (1)$$

137 where $T_{m,corr}$ is the corrected MWR temperature, $T_{m,MWR}$ is the raw T_m derived from the radiometer and α (slope) and β
138 (intercept) are the learned coefficients minimizing the residual sum of squares between the MWR and RS values. Based on
139 our training Set, the derived coefficients applied to the validation Set were $\alpha = 1.0623$ and $\beta = -15.6062$ K.

140

141 **2.2.2 Radiosonde Data Processing**

142 To establish a rigorous validation dataset, PWV was derived from high-resolution vertical profiles obtained from collocated
143 radiosonde launches. A strict collocation window was applied, where MWR profiles were averaged within ± 30 minutes of the
144 balloon launch time. The raw telemetry data, comprising pressure (P), temperature, and dew point temperature (T_d), were
145 processed to derive the total columnar water vapour content (in kg m^{-2}) through the vertical integration of specific humidity,
146 assuming the atmosphere is in hydrostatic equilibrium. The determination of the necessary moisture variables relied on the
147 Magnus-Tetens approximation, which provides a widely accepted empirical relationship for saturation vapour pressure. First,
148 the actual vapour pressure (e , in hPa) was computed directly from the dew point temperature (T_d , in $^{\circ}\text{C}$). This calculation
149 utilized the coefficients defined by Bolton (1980), which are optimized for saturation vapour pressure over liquid water in the
150 meteorological temperature range, as shown in Eq. (2):

$$151 \quad e = 6.112 \cdot \exp\left(\frac{17.67 \cdot T_d}{T_d + 243.5}\right) \quad (2)$$

152 Subsequently, the specific humidity (q , in kg kg^{-1}) was derived via Eq. (3), representing the mass mixing ratio of water vapour
153 to the total moist air parcel:

$$154 \quad q = \frac{\epsilon \cdot e}{P - (1 - \epsilon) \cdot e} \quad (3)$$

155 where P is the static pressure (hPa) and $\epsilon \approx 0.622$ represents the ratio of the molecular weight of water vapour to that of dry
156 air. Once the specific humidity profile was established, the PWV was calculated by integrating q with respect to pressure. The
157 retrieval algorithm employed the trapezoidal rule for numerical integration, which approximates the integral as the sum of
158 discrete atmospheric layers (Eq. 4):

$$159 \quad I WV = \frac{1}{g} \sum_{i=0}^{N-1} \frac{q_i + q_{i+1}}{2} \cdot |P_{i+1} - P_i| \quad (4)$$

160 where g is the gravity dependent on altitude, $g(\phi, h)$, where ϕ represents the Geodetic latitude and h is the orthometric height.
161 P is converted to Pascals (Pa) prior to integration and N represents the total number of vertical levels in the RS profile. It
162 should be noted that while the trapezoidal rule can theoretically overestimate the integral of an exponentially decaying profile,
163 the Vaisala RS41-SGP provides high-frequency 1-second telemetry (yielding a vertical spatial resolution of approximately 5
164 to 8 meters). At this exceptionally fine resolution, the linear approximation between measurement levels effectively converges
165 with the true atmospheric profile, rendering any systematic integration bias mathematically negligible. Also, it should be noted
166 that IWV, representing the mass column integral in kg m^{-2} , is physically and numerically equivalent to PWV expressed as a
167 depth in millimeters (mm), assuming the standard density of liquid water (1000 kg m^{-3}). A strict quality assurance protocol
168 was implemented to ensure vertical completeness; only radiosonde flights that successfully maintained continuous telemetry
169 up to the 10 km AGL integration ceiling were included in the final comparative dataset. While the term PWV is frequently
170 used when discussing direct profile integration from the MWR and RS, this study uses PWV (mm) as the standardized final
171 retrieval metric to align with operational meteorological and forecasting conventions. It is important to note that while the
172 nominal manufacturer uncertainty for the Vaisala RS41 humidity sensor is stated as 4 % for individual profile measurements,
173 the uncertainty of the resulting PWV is significantly lower. Because PWV is computed by integrating hundreds of discrete
174 measurements across the vertical column (Eq. 3), uncorrelated random sensor noise is largely suppressed through statistical
175 cancellation. Consequently, the integrated variables derived from the radiosonde, such as PWV and the T_m , possess the requisite
176 precision to serve as a robust 'ground truth' standard for evaluating the finer relative uncertainties (1–2 %) associated with the
177 GNSS and MWR retrievals. To ensure a rigorous and direct intercomparison with the active MWR, the radiosonde integration
178 was strictly confined to a maximum altitude of 10 km Above Ground Level (AGL). This vertical cutoff was deliberately chosen
179 to exactly match the 10 km ceiling of the standard RPG-HATPRO retrieval grid. While GNSS integrates delays through the
180 entire atmosphere, bounding the in-situ reference data is mathematically necessary to isolate profiling performance. It is well
181 established that this 10 km threshold does not introduce a systematic dry bias when comparing against total-column GNSS
182 (Van Baelen et al., 2005). Furthermore, ambient temperatures at this altitude range from $-40 \text{ }^\circ\text{C}$ to $-50 \text{ }^\circ\text{C}$, strictly limiting the
183 saturation vapour pressure. Consequently, the residual water vapour between 10 km and the tropopause is thermodynamically
184 constrained to fractions of a millimeter. Omitting this minute residual mass is functionally negligible, as it falls well within
185 the overall baseline uncertainty (typically 1–2 mm) of the total-column radiosonde PWV retrieval.

186

187 **2.2.3 GNSS Data Processing**

188 ZTD estimates were derived from the collocated Leica GR50 receiver (station NICO) using the Tefnut PP software (Douša et
189 al., 2014). The processing employed a Precise Point Positioning (PPP) strategy with an elevation cutoff angle of 10° . To
190 account for tropospheric mapping errors, the Vienna Mapping Function 1 (VMF1) was applied. Station coordinates were
191 constrained to the IGS14 reference frame, and satellite orbits and clock corrections were utilized from IGS Ultra-Rapid
192 products. While IGS Final products are the gold standard for historical climate reprocessing due to their minimal orbital

193 uncertainty, this study deliberately utilized IGS Ultra-Rapid products to evaluate the proposed synergistic retrieval architecture
 194 under near real-time operational constraints. Because a primary application of continuous GNSS-PWV is its assimilation into
 195 short-range NWP for severe weather 'nowcasting', it is crucial to assess system performance using the satellite orbits and clocks
 196 actually available during active forecasting. Although Ultra-Rapid products introduce a slight degradation in ZTD precision
 197 compared to final products, this uncertainty (typically fractions of a millimeter in PWV) remains negligible compared to the
 198 massive, multi-millimeter systematic errors introduced by static thermodynamic modeling, which is the primary focus of this
 199 investigation. While modern Numerical Weather Prediction systems frequently assimilate ZTD directly to avoid conversion
 200 uncertainties, deriving an accurate physical PWV product remains essential. PWV serves as an intuitive, absolute moisture
 201 metric heavily utilized by operational forecasters for severe weather nowcasting, and is fundamentally necessary for building
 202 long-term, cross-instrument climatological records. To isolate the ZWD, the ZHD was precisely calculated using continuous,
 203 co-located surface pressure observations obtained directly from the Vaisala WXT536 weather transmitter installed at the site,
 204 rather than relying on interpolated pressure fields. ZTD values were estimated at 15-minute intervals, directly aligning with
 205 the temporal resolution of the MWR. It must also be noted that the computation of ZHD is significantly dependent on the
 206 assumed value of the dry refractivity constant, k_1 . As established by Bevis et al. (1994) and further evaluated by Healy (2011),
 207 while k_1 is known to a high degree of relative accuracy, its residual fractional uncertainty introduces a persistent systematic
 208 bias into the ZHD estimation. Because ZWD is isolated by subtracting ZHD from the total delay, this k_1 -induced bias directly
 209 propagates into the final PWV error budget, acting alongside the conversion uncertainties analyzed later in this study.

210

211 **2.3 Thermodynamic Modeling and Synergistic Retrieval Strategy**

212 The conversion of GNSS-derived ZWD to PWV is governed by a proportionality factor, Π , whose accuracy is largely dictated
 213 by the T_m . To assess the fidelity of thermodynamic inputs for GNSS meteorology, we evaluated three distinct T_m derivation
 214 strategies. For profile-resolving instruments (MWR and RS), T_m values were computed by integrating the vertical profiles of
 215 physical temperature, $T(z)$ (K), and absolute humidity, $\rho_v(z)$ (kg m^{-3}). Consistent with Bevis et al. (1992), T_m is defined as the
 216 mean temperature of the atmosphere weighted by the water vapour partial pressure, which can be expressed in terms of vapour
 217 density as shown in Eq. (5):

$$218 \quad T_m = \frac{\int_{z_{surf}}^{z_{top}} \rho_v(z) dz}{\int_{z_{surf}}^{z_{top}} \frac{\rho_v(z)}{T(z)} dz} \quad (5)$$

219 In practice, the continuous integrals were discretized using the trapezoidal rule from the surface (z_{surf}) to the highest available
 220 profile level (z_{top}). This approach assumes linear variation of T and ρ_v between measurement levels. For standalone GNSS
 221 retrieval (where no dynamic profiles are available), T_m was derived from the HGPT2 (Hourly Global Pressure and Temperature
 222 2) model (Mateus et al., 2021). HGPT2 is an advanced 'blind' empirical model, meaning its outputs are independent of the
 223 specific observational year. While dynamic NWP models provide superior real-time meteorological data, 'blind' models like

224 HGPT2 remain heavily utilized in standard geodetic GNSS processing where real-time meteorological or NWP data streams
 225 are unavailable. It is constructed from a comprehensive 20-year historical baseline of atmospheric data from the ERA5 global
 226 reanalysis. Unlike standard static climatologies, HGPT2 leverages the full ERA5 spatial resolution (0.25°×0.25°) and provides
 227 temporal resolution at 1-hour intervals for any given Day of Year (DOY). It achieves this by employing a time-segmentation
 228 concept, modeling thermodynamic variables via long-term mean values combined with annual, semi-annual, and quarterly
 229 periodic functions.

230 Applying the linear correction model (as formulated in Section 2.2.1) successfully re-centers the error distribution. To quantify
 231 the benefits of sensor synergy in integrated water vapour estimation, this study defines and contrasts two distinct GNSS PWV
 232 retrieval architectures. The first, “Standard Retrieval” which is a control method utilizes the ZTD_{GNSS} combined with the T_m
 233 derived empirically from the HGPT2 climatological model (Böhm et al., 2015). Second “Synergistic Retrieval” which
 234 proposed method couples ZTD_{GNSS} with a physical T_m derived directly from a collocated MWR. For the synergistic approach,
 235 the dimensionless conversion factor (Π) was calculated dynamically using the MWR-derived T_m following Eq. (6) and Eq. (7).

$$236 \quad PWV = \Pi \cdot ZWD \quad (6)$$

$$237 \quad \Pi = \frac{10^6}{\rho_w R_v [k_2' + (k_3/T_m)]} \quad (7)$$

238
 239 where ρ_w represents the density of liquid water (1000 kg m⁻³) and R_v is the specific gas constant for water vapour (461.52 J
 240 kg⁻¹K⁻¹). To assess the sensitivity of the Π to the choice of thermodynamic coefficients, three widely used formulations were
 241 employed in this study, following Davis (1985)/Thayer (1974), Bevis et al. (1994), and Rüeiger (2002), as shown in Table 2:

242 **Table 2.** Refractivity constants used in the sensitivity analysis of the Π factor, based on three commonly adopted formulations.

Method	k_2 (K hPa ⁻¹)	k_3 (K ² hPa ⁻¹)	k_2' (K hPa ⁻¹)
Davis (1985) / Thayer (1974)	64.79	3.776×10 ⁵	16.52
Bevis et al. (1994)	70.40	3.739×10 ⁵	22.13
Rüeiger (2002)	71.295	3.7546×10 ⁵	22.97

243
 244 To rigorously quantify the uncertainty in the final PWV retrieval and avoid fragmented error attributions, standard error
 245 propagation must be applied to the fundamental conversion Eq. 6. Assuming the uncertainties in the wet delay and the
 246 conversion factor are uncorrelated, the variance of the final PWV (σ_{PWV}^2) is expressed using partial derivatives as in Eq. (8):

$$247 \quad \sigma_{PWV}^2 = \left(\frac{\partial PWV}{\partial ZWD}\right)^2 \sigma_{ZWD}^2 + \left(\frac{\partial PWV}{\partial \Pi}\right)^2 \sigma_{\Pi}^2 \quad (8)$$

248 Evaluating these primary partial derivatives yields the proportional contributions of the geodetic and thermodynamic
 249 components as shown in Eq. (9):

$$250 \quad \sigma_{p_{WV}}^2 = \Pi^2 \sigma_{z_{WD}}^2 + ZWD^2 \sigma_{\Pi}^2 \quad (9)$$

251 The uncertainty in the conversion factor (σ_{Π}^2) is itself a compound term driven by the T_m and the static atmospheric refractivity
 252 constants (k_2' and k_3). Its variance is defined via partial derivatives as shown in Eq. (10):

$$253 \quad \sigma_{\Pi}^2 = \left(\frac{\partial \Pi}{\partial T_m} \right)^2 \sigma_{T_m}^2 + \left(\frac{\partial \Pi}{\partial k_2'} \right)^2 \sigma_{k_2'}^2 + \left(\frac{\partial \Pi}{\partial k_3} \right)^2 \sigma_{k_3}^2 \quad (10)$$

254 The sensitivity of the conversion factor strictly to T_m (the dynamic thermodynamic variable evaluated in this study) is quantified
 255 by its partial derivative and it represented as Eq. (11):

$$256 \quad \frac{\partial \Pi}{\partial T_m} = \Pi \left[\frac{k_3}{T_m^2 \left(k_2' + \frac{k_3}{T_m} \right)} \right] \quad (11)$$

257 This consolidated formulation establishes the exact mathematical limits of thermodynamic error propagation. As demonstrated
 258 in the sensitivity analysis (Section 3.4), this framework accurately isolates the dynamic uncertainties driven by T_m from the
 259 baseline static biases introduced by the chosen refractivity constants.

260

261 **2.4 Diagnostic Parameters and Error Analysis**

262 The vertical structure of the atmosphere was analyzed by segregating the dataset into two regimes: the PBL (0-2 km), where
 263 water vapour is concentrated, and the Free Troposphere (> 2 km). Additionally, the water vapour scale height (H_v) was
 264 calculated to parameterize the vertical distribution of moisture. H_v was derived for both RS and MWR by fitting an exponential
 265 decay function (Eq. 12) to the absolute humidity profile (ρ_v).

$$266 \quad \rho_v(z) = \rho_{v,0} \cdot \exp\left(-\frac{z}{H_v}\right) \quad (12)$$

267 where $\rho_v(z)$ is the absolute humidity at height z , and $\rho_{v,0}$ is the surface humidity. This curve fitting was deliberately restricted
 268 to the lowest 4 km of the atmosphere. Because this layer contains the vast majority (>90%) of the tropospheric water vapour
 269 mass, bounding the fit prevents the algorithm from heavily weighting near-zero, noisy upper-tropospheric values that
 270 mathematically degrade the fit for the boundary layer. Furthermore, the scale height metric fundamentally assumes the
 271 atmosphere conforms to a well-behaved exponential decay. Profiles yielding H_v values outside the physically realistic range
 272 of 0.1 to 4.0 km were excluded from the statistical analysis to prevent artificial statistical skewing during complex
 273 meteorological states (e.g., deep convective mixing) where the underlying exponential model is invalid. Forcing a
 274 mathematical fit onto these non-exponential profiles yields physically meaningless artifacts. Therefore, a Quality Assurance
 275 filter was applied, bounding the analysis to the physically realistic range of $0.1 \text{ km} < H_v < 4.0 \text{ km}$. Profiles yielding values
 276 outside this range were discarded because they indicate the underlying exponential model itself is invalid for that specific
 277 atmospheric profile, preventing artificial statistical skewing in the instrument intercomparison. Profiles yielding H_v values
 278 outside the physically realistic range of 0.1 to 4.0 km were excluded from the statistical analysis. To evaluate the performance

279 limitations of standard climatological models under varying hygrometric conditions, the systematic error (ΔPWV) was defined
280 as the residual between the synergistic and standard approaches (Eq. 13):

$$281 \quad \Delta PWV = PWV_{Synergistic} - PWV_{Standard} \quad (13)$$

282 The dataset was stratified into discrete bins of 5 mm PWV to isolate regimes of moisture abundance. Within each bin, the
283 mean bias and $\pm 1\sigma$ uncertainty were computed. These statistics were utilized to determine the "Systematic Bias Threshold,"
284 defined herein as the specific hygrometric threshold where the systematic model error exceeds 1 mm. Finally, the propagation
285 of thermodynamic uncertainty into the moisture retrieval was quantified via linear regression analysis. This compared the
286 relative error in T_m (HGPT2 vs. MWR) against the resulting relative error in PWV, serving as an empirical verification of the
287 theoretical sensitivity approximation given in Eq. (14):

$$288 \quad \frac{\Delta PWV}{PWV} \approx \frac{\Delta T_m}{T_m} \quad (14)$$

289 **3 Results**

291 The following evaluation follows a top-down diagnostic approach. First, the macroscopic baseline performance of the final
292 derived moisture products is established. Subsequently, the underlying thermodynamic variables driving these discrepancies
293 are isolated, culminating in the development of a targeted calibration scheme to mitigate the identified biases.

294 **3.1 Temperature and Humidity Profile Validation**

295 MWR-retrieved temperature T and ρ_v profiles were validated against collocated RS observations at 00:00 UTC and 12:00 UTC
296 during March–October 2025. Profiles were stratified into the planetary boundary layer (PBL; 0–2 km) and free troposphere
297 (>2 km), as shown in Figs. 2 and 3. Mean vertical temperature profiles show agreement between MWR and RS (Fig. 2a–b).
298 In the boundary layer (0–2 km), MWR retrieves temperature with high precision ($r > 0.98$, $RMSE < 1.5$ K). Above 2 km, a cold
299 bias is observed in the MWR retrieval, reaching -5.16 K at 12 UTC (Fig. 2f). Despite this bias, the linearity remains strong
300 ($r \approx 0.97$), indicating the sensor captures relative thermal variations aloft despite the absolute offset. This confirms the trend
301 observed in the mean profiles, where the MWR underestimates temperatures in the mid-to-upper troposphere. Furthermore,
302 horizontal balloon drift driven by prevailing winds inevitably causes the radiosonde to sample a different atmospheric volume
303 than the MWR's strict zenith view. While this spatiotemporal mismatch introduces random scatter into the upper-level
304 comparisons, it does not artificially skew the systematic biases identified in this study. Consequently, the RMSE increases
305 substantially to approximately 6.4–6.7 °C. The stark contrast in accuracy between the lower and upper troposphere is a known
306 characteristic of ground-based microwave radiometry (Parde et al., 2025; Pakkattil et al., 2025). The high accuracy below 2
307 km is attributed to the high information content of the opaque V-band channels (51–58 GHz), whose weighting functions peak
308 near the surface. Above 2 km, these weighting functions broaden significantly, reducing vertical resolution and causing a

309 "smearing" effect where the instrument provides a volume-averaged temperature rather than a precise point measurement. The
310 observed cold bias is likely a result of the retrieval algorithm (e.g., neural network) relying heavily on a climatological *a priori*
311 dataset that does not perfectly represent the thermal conditions of the transition season observed, or systematic offsets in the
312 radiative transfer model (absorption coefficients) used for training.

313 The mean ρ_v profiles (Figs. 3a–b) show the expected exponential decrease of moisture with height. At 00 UTC, the profiles
314 align reasonably well. However, at 12 UTC, the MWR profile exhibits a structural deviation between 1–2 km, failing to capture
315 the smooth moisture gradient recorded by the RS. This discrepancy may be attributed to the MWR's limited vertical resolution
316 during periods of active daytime mixing or complex humidity layering. The retrieval of humidity in the lower atmosphere
317 shows moderate agreement but is less accurate than the temperature retrievals. Performance is notably better at night (00 UTC)
318 with r of 0.878 and RMSE of 1.98 g m^{-3} . At 12 UTC, the correlation drops to 0.744, and the scatter increases (RMSE = 2.31 g
319 m^{-3}). Because the integrated mass of the water vapour column is physically and numerically equivalent to its depth (assuming
320 the standard density of liquid water), this physical quantity is exclusively referred to as PWV expressed in millimeters (mm)
321 throughout this study to align with operational meteorological conventions. A negative bias persists at both times (-0.51 g m^{-3}
322 at 00 UTC and -0.91 g m^{-3} at 12 UTC), indicating a tendency for the MWR to underestimate moisture content in the boundary
323 layer, particularly during the day. Surprisingly, the statistical linearity for ρ_v improves slightly or remains stable above 2 km,
324 likely due to the lower overall magnitude of humidity at these heights. The correlation coefficients remain stable (~ 0.87). In
325 contrast to the lower levels, the bias shifts to slightly positive values (0.23 g m^{-3} at 00 UTC and 0.46 g m^{-3} at 12 UTC),
326 suggesting a slight moist bias in the MWR retrievals aloft. The linear fits (Figs. 3e–f) align closely with the 1:1 line, with
327 slopes near unity (0.90 and 1.00), indicating that the MWR effectively captures the free tropospheric humidity trends despite
328 the lower absolute values. The difficulty in retrieving accurate ρ_v profiles, particularly at 12 UTC, stems from the limited
329 vertical resolution of the K-band channels (22–31 GHz). Unlike temperature profiling, humidity profiling offers very few
330 independent degrees of freedom (typically < 3), making it difficult for the MWR to resolve sharp vertical gradients often present
331 at the top of the convective boundary layer during the daytime. The structural deviation and underestimation are common
332 issues linked to the "smoothing" error inherent in passive radiometry, where sharp moisture inversions are averaged out.
333 Furthermore, the persistent bias suggests potential uncertainties in the water vapour absorption models (spectroscopic
334 parameters) or non-representative training data used in the retrieval algorithm.

335

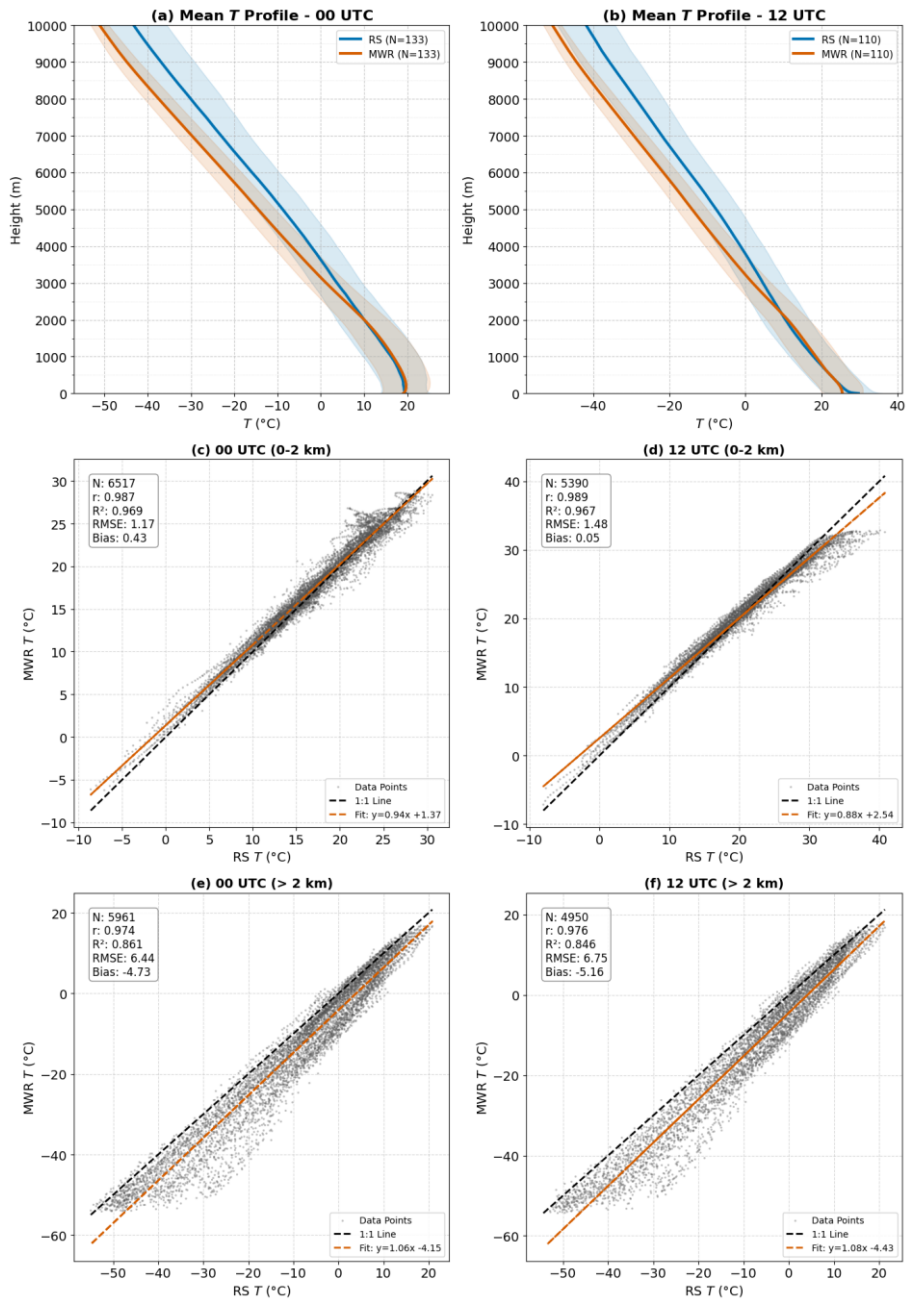


Figure 2. Comparison of radiosonde and microwave radiometer (MWR) temperature profiles: (a–b) Mean vertical temperature (T) profiles at 00 and 12 UTC with variability shading; (c–f) Scatter comparisons for the lower (0–2 km) and upper (>2 km) atmosphere at both times.

336
337
338
339

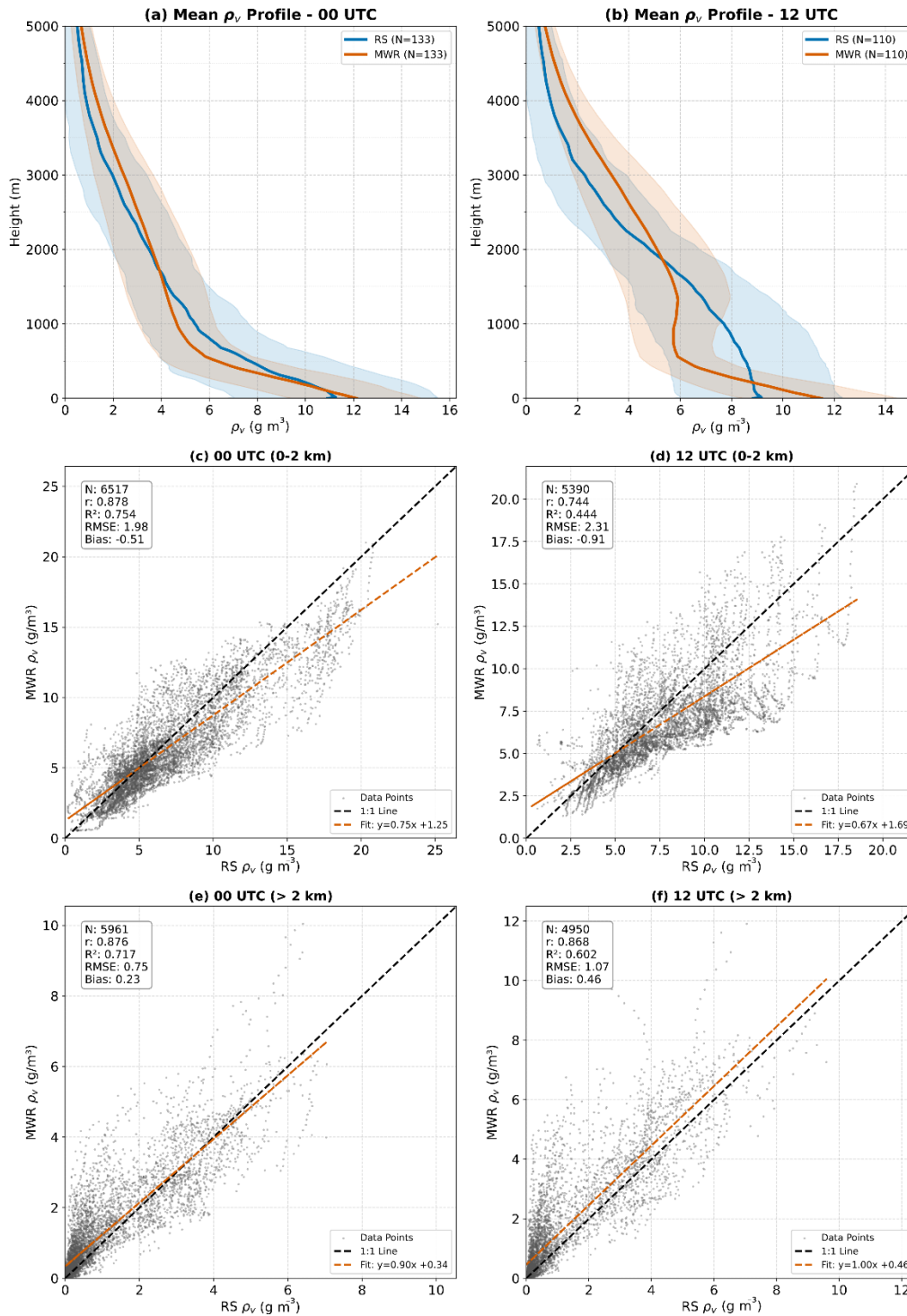


Figure 3. Comparison of radiosonde and microwave radiometer (MWR) absolute humidity (ρ_v) profiles: (a–b) Mean vertical ρ_v profiles at 00 and 12 UTC with variability shading; (c–f) Scatter comparisons for the lower (0–2 km) and upper (>2 km) atmosphere at both times.

340
 341
 342
 343

3.2 Precipitable Water Vapour (PWV) and Scale Height (H_v) Validation

Unlike vertical profiling, the MWR excels in measuring total column quantities. The comparison with RS yields an excellent correlation ($r=0.971$) and a low RMSE of 1.72 kg m^{-2} . This performance disparity—superior PWV versus degraded profiles—confirms that while the sensor cannot resolve vertical structural details due to smoothing error, the radiometric brightness temperature in the K-band remains strictly proportional to the total precipitable water mass. The GNSS-derived PWV shows a slight negative bias relative to RS (-0.45 kg m^{-2}), whereas it relative to the MWR exhibits a positive bias ($+0.45 \text{ kg m}^{-2}$). The cumulative offset observed in the MWR-GNSS intercomparison ($+0.89 \text{ kg m}^{-2}$) highlights the systematic differences in calibration and retrieval assumptions between active (GNSS) and passive (MWR) techniques. The GNSS underestimation is likely driven by errors in the T_m derived from the static HGPT2 model, a hypothesis further explored in Section 3.4. To further diagnose the structural limitations of the retrievals, we evaluated the water vapour H_v . While H_v is admittedly a single-parameter representation of the complex atmospheric moisture profile, it is a crucial parameter that provides a representative value for the rate at which water vapour decreases with altitude—a key factor in understanding atmospheric stability, cloud formation, and radiative transfer processes. In this study, it is utilized specifically as a diagnostic metric to quantify the vertical structural limitations of passive microwave remote sensing. The comparison of H_v calculated from RS and MWR profiles is shown in Fig. 5. Unlike the high-fidelity PWV retrievals, the MWR-derived scale height shows negligible correlation with RS observations ($r=0.25$, $R^2=-2.87$) and a massive systematic positive bias of 0.62 km . The histograms (Fig. 5b) further elucidate this discrepancy: while the RS scale heights follow a narrow, physically realistic distribution centered around a mean (μ) of 1.51 km , the MWR distribution is artificially broad and shifted to significantly higher values ($\mu=2.13 \text{ km}$).

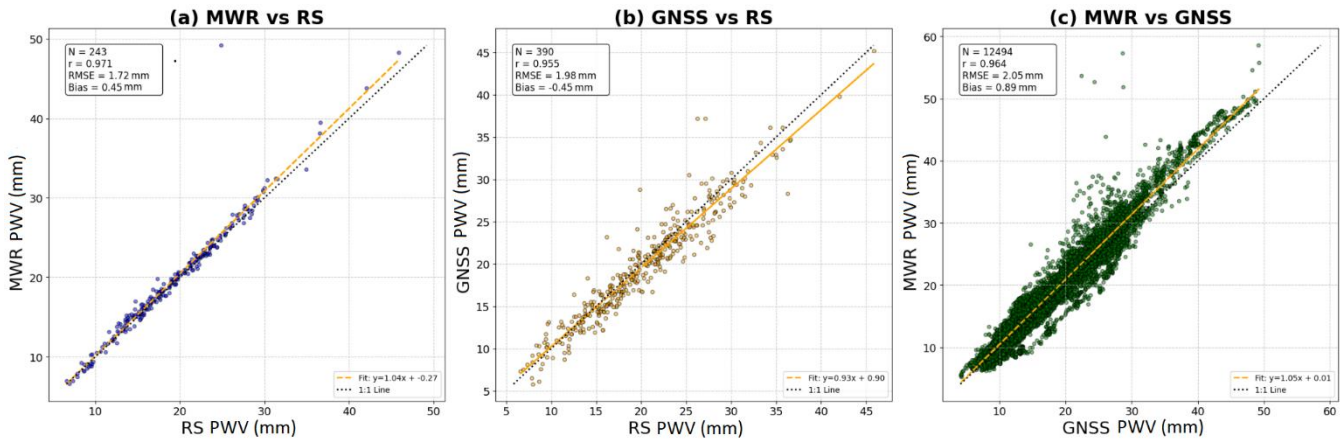
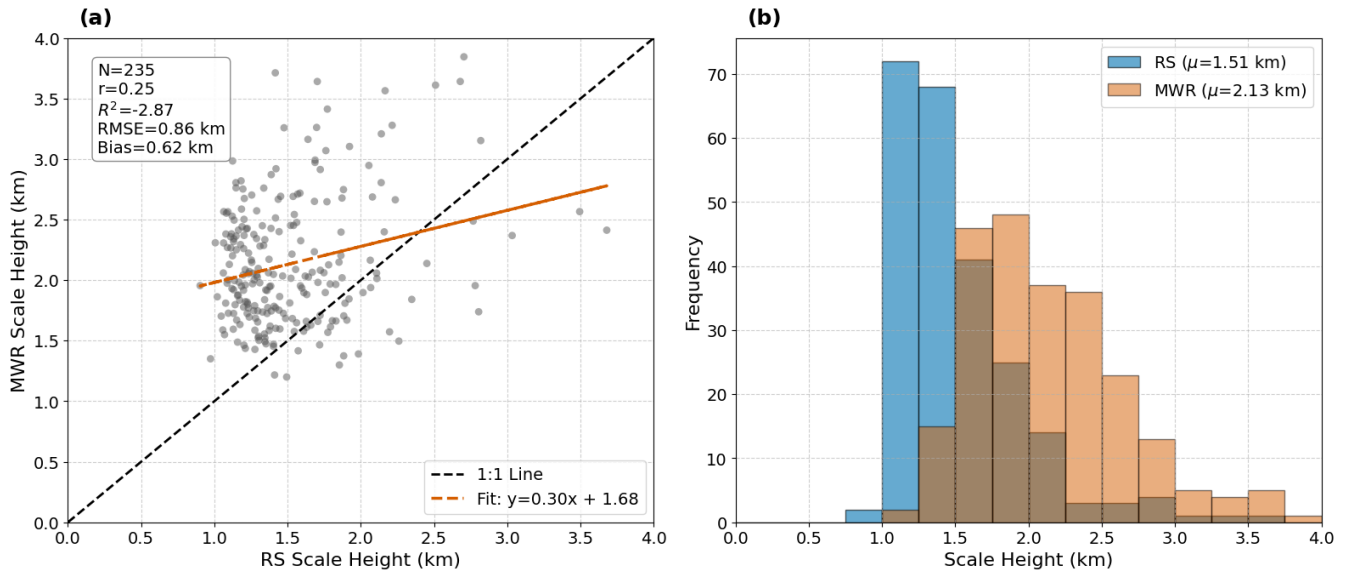


Figure 4. Intercomparison of precipitable water vapour (PWV) retrieved from Microwave Radiometer (MWR), GNSS, and Radiosonde observations. (a) MWR PWV versus radiosonde PWV, (b) GNSS PWV (derived using HGPT2 T_m) versus radiosonde PWV, and (c) MWR PWV versus GNSS PWV (derived using HGPT2 T_m).

The large scatter and ambiguity in the MWR estimates—which completely dwarf the individual least-squares fit uncertainties of the exponential regression—are a direct consequence of the instrument's physical limitations. H_v is highly sensitive to the sharp vertical gradient of humidity at the top of the planetary boundary layer. However, the K-band channels

370 (22–31 GHz) utilized for humidity profiling possess broad weighting functions, restricting the vertical degrees of freedom to
 371 typically fewer than three. Because the MWR lacks the vertical resolution to capture sharp moisture inversions, the retrieval
 372 algorithm mathematically smears the moisture mass upward. This inherent 'smoothing error' artificially elongates the vertical
 373 moisture profile, effectively inflating the calculated e-folding depth. Therefore, the inclusion of this H_v analysis serves to
 374 transparently demonstrate a critical operational boundary: while the MWR is an excellent standard for PWV, it is significantly
 375 unreliable and mathematically unsuited for characterizing vertical moisture compactness. The significant deviations observed
 376 in these macroscopic retrieval products necessitate a deeper investigation into the intermediate thermodynamic variables
 377 driving the conversion process. Consequently, the isolated performance of the T_m is evaluated in Section 3.3, followed by the
 378 introduction of a post-retrieval MWR calibration scheme in Section 3.4 designed to mitigate these native biases.

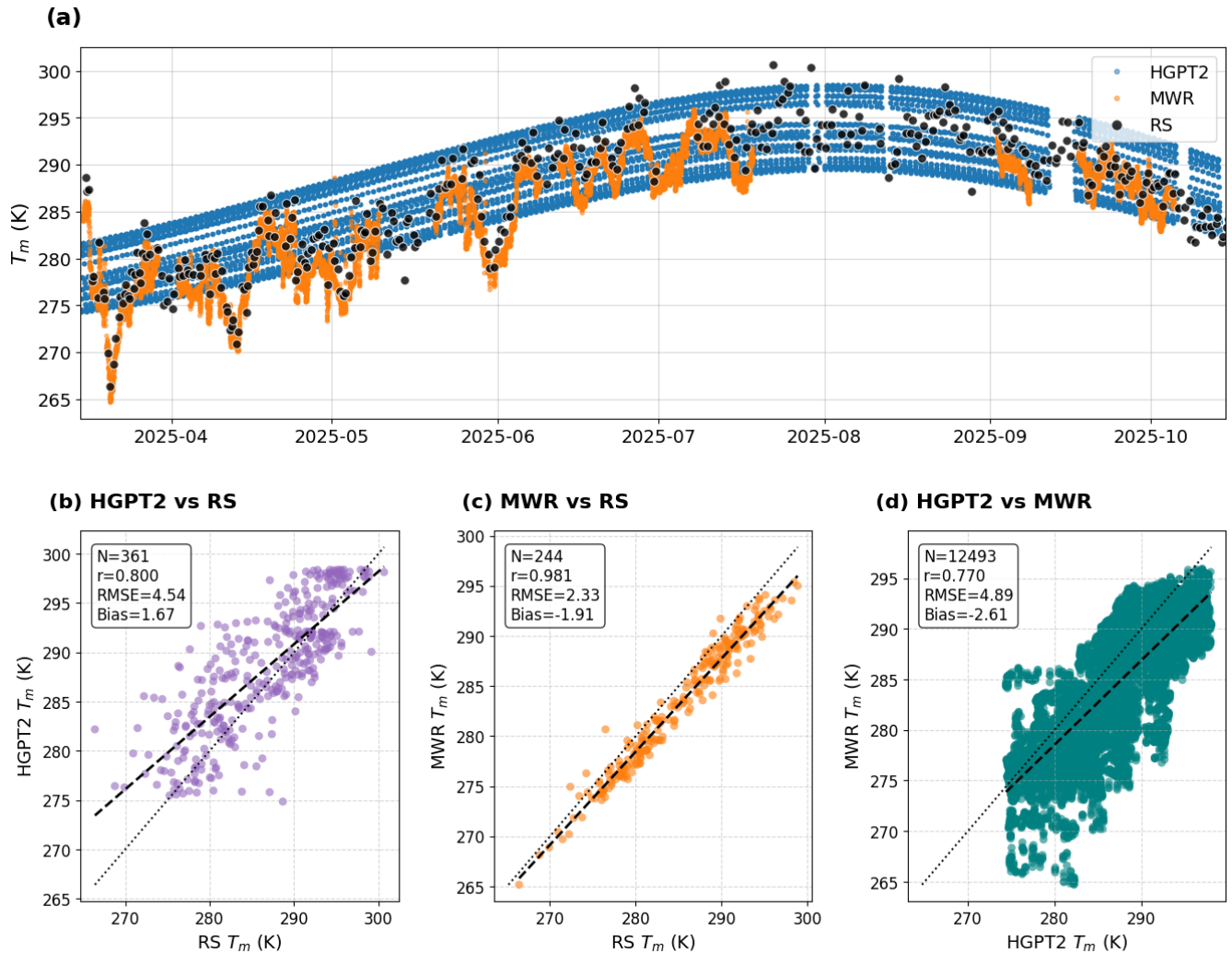


379 **Figure 5:** Comparison of scale height from radiosonde (RS) and microwave radiometer (MWR): (a) Scatter plot with 1:1 line and linear fit,
 380 including summary statistics; (b) Frequency distributions showing mean scale heights for RS and MWR.
 381
 382

383 3.3 Weighted Mean Temperature (T_m) Validation

384 The accurate estimation of the T_m is critical for converting GNSS-derived ZWD into PWV. The performance of T_m derived
 385 from the MWR and the empirical GPT2w model (HGPT2) was evaluated against RS measurements, which serve as the "ground
 386 truth." The results are presented in Fig. 6. The time series (Fig. 6a) illustrates the seasonal evolution of T_m from April to October
 387 2025. The Radiosonde observations (black dots) show significant variability, capturing synoptic-scale weather fluctuations.
 388 The MWR-derived T_m (orange dots) tracks these fluctuations with remarkable precision, overlaying the RS points almost
 389 perfectly. In stark contrast, the HGPT2 model (blue dots) provides a smooth, climatological curve. While it captures the general
 390 seasonal trend, it completely misses the day-to-day thermodynamic variability, often overestimating T_m during cooler transient
 391 events and underestimating it during warmer anomalies. The empirical model shows only moderate performance ($r=0.800$)

392 with a substantial spread (RMSE = 4.54 K). A systematic positive bias of 1.67 K indicates that HGPT2 generally overestimates
393 the atmospheric temperature profile in this region. The scatter plot reveals a diffuse, "cloud-like" distribution, confirming its
394 inability to capture real-time atmospheric dynamics. The MWR demonstrates superior performance, achieving a near-perfect
395 correlation ($r=0.981$). The RMSE is significantly reduced to 2.33 K, which is nearly half the error of the empirical model.
396 Interestingly, the MWR exhibits a negative bias of -1.91 K, suggesting a systematic underestimation of T_m . Crucially, this bias
397 does not originate in the free troposphere, but rather in the planetary boundary layer (0–3 km). Since T_m is weighted by water
398 vapour pressure, this "cold bias" indicates the MWR is underestimating the intense near-surface heating or the sharp lapse
399 rates characteristic of the Nicosia environment. Despite this offset, the tight linearity indicates that MWR is an excellent source
400 for capturing real-time T_m variations. Comparing the large dataset of MWR against HGPT2 ($N=12,493$) confirms the
401 discrepancy between dynamic and static modeling. The correlation is lower ($r=0.770$) and the scatter is large (RMSE = 4.89
402 K), further proving that static empirical models are insufficient for high-precision GNSS meteorology compared to dynamic
403 radiometer measurements. While errors in ZTD estimation contribute significantly to the overall uncertainty budget, the
404 specific error introduced during the conversion from delay to water vapour is linearly dependent on the accuracy of T_m .
405 Assuming a given ZTD, a standard rule of thumb states that a 1 % relative error in T_m translates to roughly a 1 % relative error
406 in the resulting PWV. By switching from a static model (HGPT2, ~ 4.5 K error) to a dynamic sensor (MWR, ~ 2.3 K error),
407 the uncertainty in the GNSS water vapour product is effectively halved. This validates the "synergistic" approach of using
408 collocated MWR thermal data to process GNSS signals.



409
 410 **Figure 6.** Comparison of weighted mean temperature (T_m) derived from HGPT2, MWR, and Radiosonde (RS) during March–November
 411 2025. (a) Time series of T_m estimates from all three sources. (b–d) Scatter plots showing statistical comparisons between: (b) HGPT2 vs.
 412 RS, (c) MWR vs. RS, and (d) HGPT2 vs. MWR.

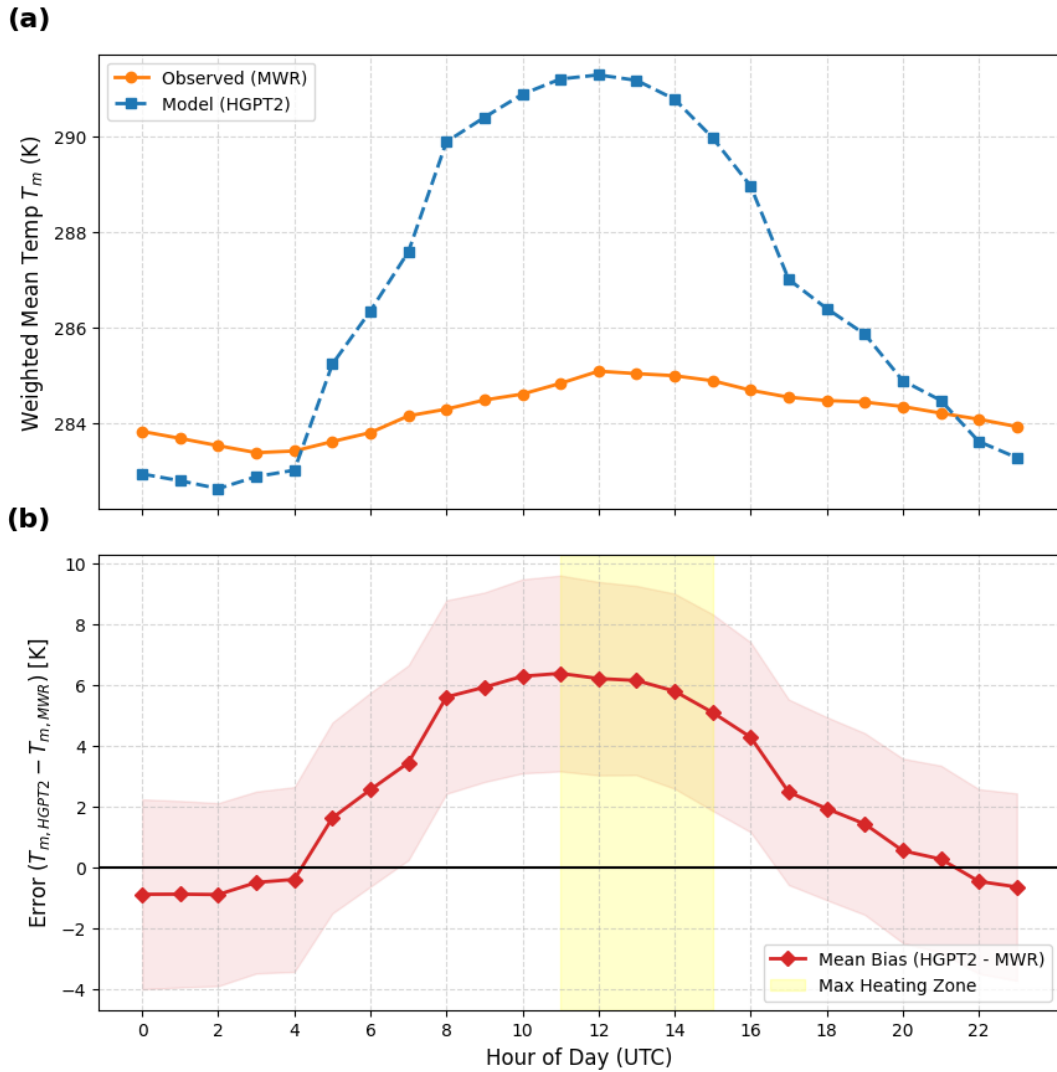
413
 414 **3.4 Diagnostic Analysis of Thermodynamic Conversion Uncertainty**

415 **3.4.1 Diurnal Bias Amplification in Static Models**

416 To pinpoint the physical origin of the HGPT2 model's deficiency, a diurnal cycle analysis was performed (Fig. 7). While the
 417 previous statistical metrics indicated a general positive bias, the temporal breakdown in Fig. 7a reveals that this error is not
 418 uniform, but is driven by a fundamental misrepresentation of atmospheric thermodynamics. The MWR-derived T_m (orange
 419 line) exhibits a physically realistic, dampened diurnal amplitude of approximately 1.5 K. This stability reflects the high thermal

420 inertia of the tropospheric column, which does not heat rapidly in response to surface insolation. In stark contrast, the HGPT2
421 model (blue line) displays an exaggerated diurnal wave with an amplitude exceeding 8.5 K, peaking synchronously with solar
422 noon (12:00 UTC). As previously documented in the literature (Wang, 2005; Bock, 2021), deriving T_m via empirical regression
423 on surface temperature (T_s) is known to introduce spurious diurnal cycles. Our observations confirm this intrinsic limitation:
424 because the empirical model's periodic functions are overly sensitive to T_s , it assumes intense surface-level heating propagates
425 uniformly through the column, failing to capture the true thermodynamic decoupling between the turbulent planetary boundary
426 layer and the stable free troposphere. During the hours of peak solar insolation (11:00–14:00 UTC), the coastal environment
427 experiences active convective mixing and the onset of the sea breeze, which dramatically alters the vertical distribution of
428 water vapour. If the underlying reanalysis climatology fails to adequately resolve the sharp moisture capping inversion at the
429 top of the daytime planetary boundary layer (PBL), it will misrepresent the T_m weighting function. Specifically, if the model
430 traps too much moisture near the intensely heated surface—or fails to capture the thermodynamic decoupling between the
431 turbulent PBL and the stable free troposphere — the integral will disproportionately weight the hottest atmospheric layers.
432 This coupled temperature-humidity mechanism physically manifests as the severe diurnal bias peak effect observed in Fig. 7b,
433 where the systematic bias surges to over +6 K. This demonstrates that high-precision GNSS meteorology requires synergistic
434 MWR data to capture both the true thermal stability and the dynamic vertical moisture weighting of the atmosphere.

435



436
437
438
439
440

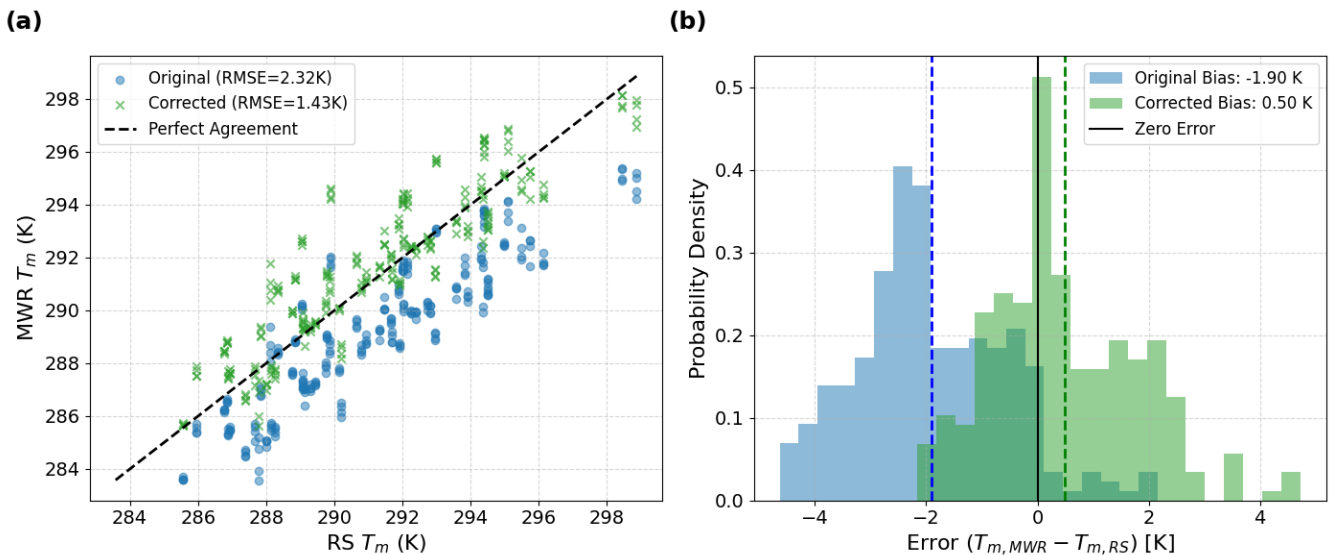
Figure 7. Diurnal variation of weighted mean atmospheric temperature T_m derived from microwave radiometer (MWR) observations and HGPT2 model simulations (top panel). The bottom panel shows the corresponding hourly mean bias $(T_{m,HGPT2} - T_{m,MWR})$, with shaded envelopes indicating variability. The yellow shaded region highlights the period of maximum daytime heating.

441 3.4.2 Calibration and Bias Correction of MWR T_m

442 Fig. 8 presents a statistical validation of the MWR derived T_m against co-located RS observations. The analysis highlights the
443 necessity and efficacy of a linear bias correction scheme to improve GNSS-PWV conversion accuracy. The scatter plot (Fig.
444 2a) reveals a distinct systematic deviation in the original MWR retrieval relative to the RS reference. The data points
445 consistently fall below the 1:1 identity line, indicating a negative bias in the raw MWR T_m product. The original RMSE is 2.32
446 K. This error is largely driven by the systematic offset rather than random scatter, as evidenced by the high linearity (R^2) of

447 the relationship. The thermodynamic profiles were retrieved using the manufacturer's standard Neural Network (NN)
 448 algorithm, trained on Region historical RS data.

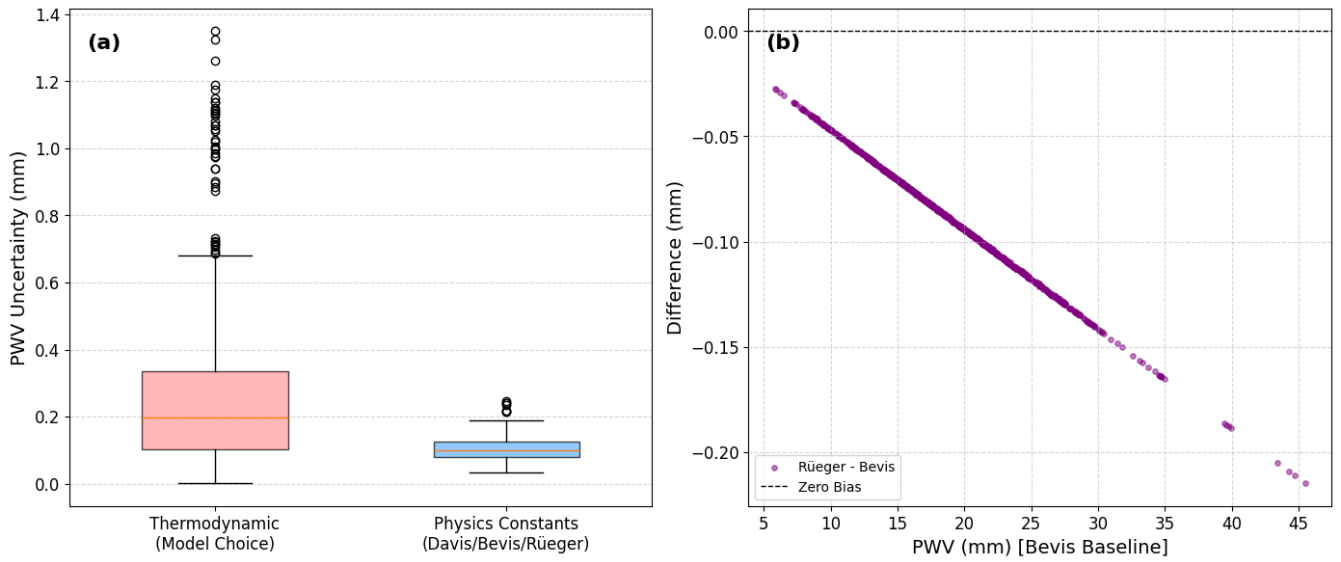
449 The Probability Density Function (PDF) of the errors ($T_{m,MWR} - T_{m,RS}$) in Fig. 8b clearly visualizes the bias shift. The pre-
 450 correction distribution is non-Gaussian and shifted significantly to the negative domain, with a mean bias (μ) of -1.90 K. In
 451 the context of GNSS meteorology, a T_m error of ≈ 2 K translates to a relative PWV error of approximately 0.7–1.0 %. For
 452 climate monitoring, this represents a significant systematic dry bias. Applying the linear correction model (as formulated in
 453 Section 2.2.1) successfully re-centers the error distribution. The post-correction bias is reduced to 0.50 K, and the histogram
 454 aligns symmetrically around the zero-error line. The correction reduces the RMSE to 1.43 K, which is consistent with the
 455 theoretical accuracy limit of ground-based radiometric profiling (typically 1–2 K). The remaining spread (width of the green
 456 histogram) represents the random error component, likely attributable to instrumental noise and the imperfect spatiotemporal
 457 matching between the instantaneous MWR zenith view and the drifting radiosonde balloon. The correction methodology
 458 effectively removes the systematic instrumental bias without artificially compressing the natural variability of the atmosphere.
 459 The reduction of RMSE by ~ 38 % (from 2.32 K to 1.43 K) confirms that site-specific calibration of T_m is a mandatory
 460 processing step for generating climate-quality GNSS-PWV datasets.



461
 462 **Figure 8.** Evaluation of weighted mean temperature T_m correction against Radiosonde (RS) observations. (a) scatter plots of original and
 463 bias-corrected MWR-derived T_m versus RS T_m with the dashed line indicating perfect agreement. (b) presents the probability density of
 464 errors ($T_{m,MWR} - T_{m,RS}$) before and after correction, demonstrating a substantial reduction in cold bias and RMSE.
 465

466 3.4.3 Uncertainty Budget Analysis

467



468 **Figure 9.** (a) PWV uncertainty attributed to thermodynamic assumptions and to the choice of refractivity constants. (b) Difference in GNSS-
 469 derived PWV resulting from the use of alternative refractivity constant formulations relative to Bevis et al. (1994).
 470

471
 472 In standard GNSS network processing, the largest source of PWV uncertainty is often the interpolation or modeling of
 473 surface pressure required to calculate the ZHD (Van Malderen et al., 2022). However, the CYGMEN observatory setup
 474 mitigates this spatial interpolation error by utilizing the co-located Vaisala WXT536 sensor, which has a stated pressure
 475 accuracy of ± 0.5 hPa. A 0.5 hPa pressure uncertainty propagates to approximately 1.15 mm of error in the ZHD. After applying
 476 the Π conversion factor, this restricts the pressure-induced PWV uncertainty to roughly ± 0.17 mm. Because this high-precision
 477 localized pressure data effectively minimizes ZHD uncertainty, the accuracy of the T_m parameterization emerges as the
 478 dominant remaining variable in the PWV error budget for this site.

479 It is important to note that the complete error budget for GNSS-derived PWV encompasses significant uncertainties
 480 originating from the ZTD estimation phase itself. These include geodetic errors such as satellite orbit and clock uncertainties,
 481 mapping function inaccuracies, and site-dependent electromagnetic effects like signal scattering and multipath. While these
 482 geodetic factors are critical, the following component-wise uncertainty analysis (Fig. 9) specifically isolates the errors
 483 introduced during the subsequent conversion step (Π). To decouple these retrieval contributions, two primary sources of
 484 uncertainty were isolated: the thermodynamic parameterization of T_m and the selection of atmospheric refractivity constants
 485 (k_2' , k_3). When decoupling these retrieval contributions, it is critical to distinguish between the statistical nature of the
 486 underlying error sources. As demonstrated by Healy (2011), uncertainties in the atmospheric refractivity constants (k_2' , k_3) act
 487 strictly as static systematic biases; selecting a different set of published constants permanently shifts the baseline of the Π by
 488 a fixed margin. Conversely, the uncertainty originating from the T_m parameterization is a dynamic, compound error. As
 489 highlighted by Wang et al. (2005) and Bock et al. (2021), empirical T_m models derived from surface temperatures often fail to

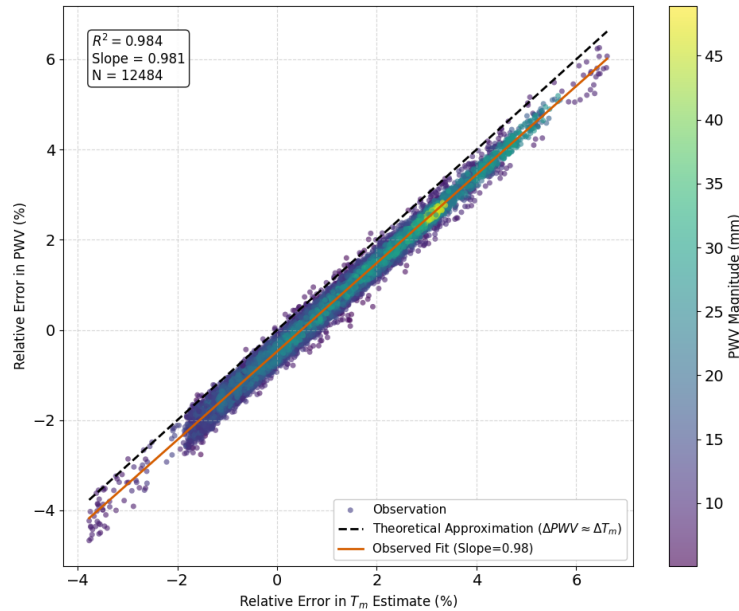
490 capture the true profile variance, introducing both a systematic bias (the model's mean regional offset) and a substantial random
 491 error component (the statistical scatter, or RMSE, driven by real-time thermodynamic variability and diurnal decoupling).
 492 While Fig. 9 juxtaposes these two distinct sources to illustrate their relative bounding magnitude on the final PWV product,
 493 their significantly different statistical behaviors—static bias versus dynamic scatter—must be acknowledged. As illustrated in
 494 Fig. 9(a), and explicitly evaluating the components of the conversion uncertainty framework established in Eq. (10), the
 495 variance introduced by the T_m estimation strategy ($\sigma_{T_m}^2$) significantly outweighs the influence of the physical constants
 496 ($\sigma_{k_2}^2, \sigma_{k_3}^2$). Feeding our empirically derived thermodynamic uncertainties into the partial derivative formulation defined in Eq.
 497 (11) specifically, substituting the HGPT2 RMSE of 4.54 K versus the corrected MWR RMSE of 1.43 K as our σ_{T_m} values—
 498 yields an isolated PWV retrieval error of approximately 1-2 mm due to stochastic thermodynamic variability. In contrast,
 499 evaluating the exact mathematical limits of the refractivity coefficients ($\sigma_{k_2}, \sigma_{k_3}$) defined here as the maximum divergence
 500 between the historical Davis et al. (1985), the standard Bevis et al. (1994), and the updated Rüeiger (2002) formulations—
 501 results in an uncertainty an order of magnitude smaller. Fig. 9(b) further resolves the impact of the refractivity constants,
 502 showing the differential bias between the oldest (Davis) and newest (Rüeiger) standards. The relationship is linear and
 503 proportional to the total water vapour content, consistent with a scaling of the Π factor. While the transition to the Rüeiger
 504 (2002) constants introduces a systematic positive shift, the magnitude of this correction (typically <0.2 mm for standard
 505 loading) is negligible for synoptic meteorological applications compared to the noise induced by T_m errors. However, for long-
 506 term climatological trend analysis where stability is paramount, consistent adherence to the Rüeiger (2002) standard is
 507 recommended to eliminate this small, but persistent systematic bias. Overall, the correction of the T_m is 2.5 times more
 508 important than selection of the constant.

509

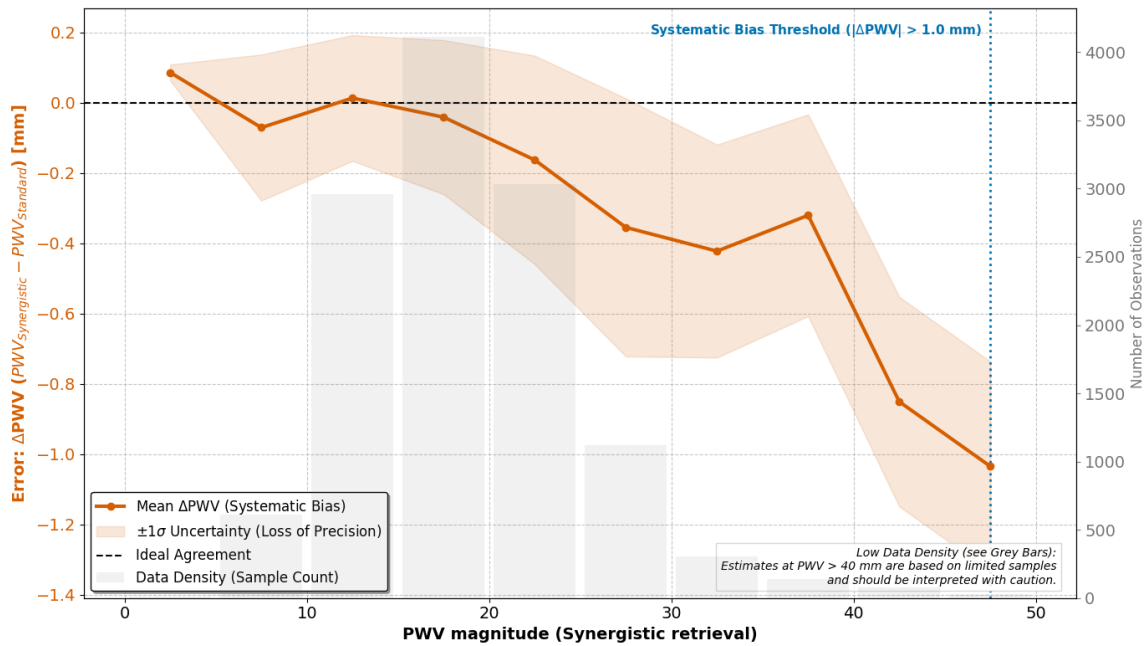
510 **3.5 Error Propagation and Synergistic Retrieval Assessment**

511 In this section, the PWV was derived using bias-corrected mean temperature (T_m) and constant values based on the study by
 512 Rüeiger (2002), as mentioned in the Sect. 3.4. The impact of T_m errors on the final PWV product was analyzed to quantify the
 513 benefits of the synergistic retrieval method. Fig. 10 visualizes the direct relationship between the relative error in T_m and the
 514 resulting relative error in PWV. The plot reveals a strictly linear relationship ($R^2=0.984$) with a slope of 0.981. This confirms
 515 the theoretical approximation that $(\Delta PWV/PWV) \approx (\Delta T_m/T_m)$. The color gradient indicates that this linear error propagation
 516 holds true across all PWV magnitudes (from <10 mm to >45 mm). This implies that temperature errors propagate directly into
 517 moisture errors regardless of the humidity level, making accurate T_m crucial at all times. Fig. 11 investigates the systematic
 518 difference (ΔPWV) between the synergistic retrieval (using MWR T_m) and a standard retrieval (using empirical T_m) as a function
 519 of moisture abundance (PWV magnitude). For drier conditions (PWV < 25 mm), the difference is minimal (near zero), and
 520 the uncertainty (shaded region) is low. This suggests that for low humidity, the choice of T_m source is less critical. As
 521 atmospheric moisture increases (> 25 mm), a significant negative bias emerges. The curve dips sharply, reaching nearly -1.0

522 mm at extreme humidity (45+ mm). The 'Systematic Bias Threshold' marker indicates that beyond 45 mm, the discrepancy
 523 exceeds 1.0 mm. The fact that the bias magnitude scales directly with total PWV provides physical confirmation that the error
 524 source is located in the boundary layer, where the bulk of the water vapour resides. The growing negative bias demonstrates
 525 that standard GNSS processing (using static models like HGPT2) systematically overestimates water vapour during extreme
 526 events compared to the more accurate synergistic method. Rather than extrapolating these localized errors to regional
 527 hydrological impacts, we emphasize the primary empirical observation: the systemic deviation of the standard empirical model
 528 scales proportionally with the magnitude of the PWV regime. Crucially, this systematic overestimation of moisture during
 529 extreme events is deeply intertwined with the diurnal cycle of the local atmosphere. This analysis quantifies the specific
 530 operational penalty of utilizing static climatological models in this region, demonstrating that HGPT2 incurs an PWV error
 531 exceeding 1.0 mm during severe thermodynamic events. As previously established (Fig. 7), the static HGPT2 model displays
 532 an exaggerated diurnal wave with an amplitude exceeding 8.5 K. Because the static model fails to account for the
 533 thermodynamic decoupling between the heated boundary layer and the cooler free troposphere during the day, this T_m error
 534 artificially inflates the amplitude of the GNSS-derived PWV diurnal cycle during peak solar insolation. By utilizing the
 535 synergistic retrieval approach, this spurious daytime moisture amplification is effectively mitigated. While further multi-site,
 536 long-term studies are required to assess the broader impacts on regional operational forecasting, our localized dataset clearly
 537 indicates that integrating real-time MWR thermal data successfully removes diurnal artifacts and reduces systematic
 538 measurement biases at this site.



539 **Figure 10.** Driver of model failure: Impact of weighted mean temperature (T_m) accuracy on PWV retrieval.
 540
 541
 542



543
544
545

Figure 11. Systematic breakdown and instability of the Standard GNSS model under extreme thermodynamic conditions.

546 **4 Discussions**

547 The results of this study necessitate a fundamental re-evaluation of how T_m parameterization errors are parameterized in GNSS
548 meteorology, particularly within thermodynamically complex, semi-arid coastal environments like the Eastern Mediterranean.
549 The pronounced failure of the static HGPT2 model to capture the diurnal T_m cycle reveals a structural limitation inherent to
550 empirical modeling. The observed "diurnal bias peak" effect is not merely a statistical anomaly; it represents a physical
551 disconnect. Static empirical models rely heavily on T_s , effectively assuming that intense surface-level heating propagates
552 uniformly through the atmospheric column. This assumption critically breaks down during the daytime in the EM, where the
553 turbulent planetary boundary layer (PBL) aggressively decouples from the stable free troposphere. Evidence for this severe
554 decoupling is explicitly documented in the high-vertical-resolution RS profiles collected during the campaign. Because the
555 passive MWR struggles to effectively capture this sharp boundary—a direct result of the broad weighting functions and
556 degraded vertical resolution inherent to its K-band observations—the instrument exhibits a 'smoothing error' across the
557 inversion layer. This structural limitation highlights exactly why applying a site-specific bias correction to the MWR's native
558 output is a necessary prerequisite for precision GNSS meteorology. Furthermore, the failure of the reanalysis climatology to
559 properly resolve the sharp moisture capping inversion during the onset of the daytime sea-breeze significantly corrupts the
560 moisture-weighted T_m integral. Ground-based microwave radiometry overcomes this structural blindness by directly measuring
561 the integrated thermal emissions of the column.

562 However, the performance of the MWR in this study highlights the duality of passive microwave remote sensing: it is highly
563 proficient at retrieving integral quantities but degrades severely when resolving differential or gradient-based parameters. The
564 successful reduction of the T_m RMSE via site-specific linear correction confirms that the MWR's K-band and V-band channels
565 effectively capture the true thermal inertia of the troposphere. The initial systematic cold bias observed aloft is a known artifact
566 of ill-posed neural network retrievals (Cimini et al., 2006; Löhnert and Maier, 2012). Because the vertical resolution of passive
567 microwave observations degrades rapidly with height, the retrievals become heavily constrained by historical training datasets
568 (the climatological prior), which often fail to capture localized, transition-season lapse rates in the free troposphere.
569 Conversely, the complete failure of the MWR to derive a physically realistic water vapour scale height (H_v) exposes the
570 "smoothing error" inherent to passive radiometry. Because the broad weighting functions of the K-band channels cannot
571 resolve sharp boundary layer moisture inversions, the retrieval algorithm mathematically smears the moisture mass upward.
572 This confirms that while MWR serves as a robust standard for total column mass, researchers must exercise extreme caution
573 when utilizing its smoothed profiles to characterize vertical moisture compactness.

574 While this study relies on a single-site, multi-month dataset, the physical mechanisms identified have broad relevance beyond
575 the Nicosia region. The Eastern Mediterranean serves as a highly representative climatic hotspot for semi-arid coastal
576 environments experiencing enhanced warming and intensified hydrological cycles. It is important to note that the specific
577 threshold of >45 mm identified here is characteristic of the climatological moisture capacity of the Eastern Mediterranean
578 during extreme summer anomalies. While the exact numerical value of this 'Systematic Bias Threshold' will vary
579 geographically depending on local atmospheric dynamics and latitude, the underlying physical principle remains universal:
580 empirical T_m models systematically degrade proportionally to the total atmospheric moisture mass during severe local
581 extremes. The core vulnerability exposed in this research—that static global models are structurally blind to sharp boundary
582 layer thermodynamic decoupling during peak insolation—is a fundamental physics problem, not a local anomaly. Therefore,
583 the proposed synergistic MWR-GNSS retrieval architecture provides a universally applicable solution for mitigating
584 systematic dry biases in any complex terrain or coastal environment globally. While the simple linear regression applied in
585 this study proved highly effective at correcting systematic T_m biases for operational GNSS conversions, there remains room
586 for algorithmic improvement. As the CYGMEN infrastructure accumulates a multi-year climatological database of high-
587 resolution radiosonde profiles, future work should focus on complementary Neural Network (NN) training. By retraining the
588 MWR retrieval algorithms using site-specific radiative transfer modeling rather than relying on the manufacturer's regional
589 historical priors, the native temperature and humidity profiles can be further optimized at the retrieval level.

590 Finally, our component-wise uncertainty analysis clarifies the error propagation chain in the GNSS-PWV conversion
591 process, shifting the paradigm of where optimization efforts should be focused. Historically, significant effort within the
592 geodetic community has been expended on refining atmospheric refractivity constants. However, we demonstrate that the error
593 induced by transitioning from the historical Davis et al. (1985) formulations to the modern Rüeiger (2002) constants is

594 practically negligible (<0.2 mm) for synoptic meteorological applications. The true "weak link" in the retrieval chain is
595 unequivocally the thermodynamic parameterization, which introduces errors an order of magnitude larger.

596

597 **5 Conclusion**

598 This study demonstrated that the accuracy of GNSS-derived Precipitable Water Vapour (PWV) in the Eastern Mediterranean
599 region, is significantly affected by the thermodynamic rigidity of static climatological models. By implementing a synergistic
600 retrieval strategy that couples GNSS delays with real-time ground-based microwave radiometry (MWR), we successfully
601 quantified and mitigated these limitations. The investigation yielded three primary methodological conclusions. First, we
602 established that standard empirical models (e.g., HGPT2) are structurally incapable of resolving the diurnal thermodynamic
603 decoupling between the boundary layer and free troposphere. This deficiency leads to severe systematic errors (the "diurnal
604 bias peak" effect) exceeding 6 K in weighted mean temperature (T_m) during peak solar insolation, which directly propagates
605 into a PWV bias >1.0 mm during extreme hygrometric events. Second, the MWR proved to be a superior source for T_m
606 parameterization errors, provided that site-specific calibration is applied. The development of a linear bias correction scheme
607 reduced the MWR T_m root-mean-square error from 2.32 K to 1.43 K. This correction substantially reduces the conversion-
608 related uncertainty in the GNSS water vapour product compared to standard climatological approaches. Third, the component-
609 wise sensitivity analysis confirmed that thermodynamic parameterization is a highly significant source of uncertainty that
610 exacerbates existing geodetic ZTD errors, outweighing uncertainties in refractive index constants by an order of magnitude.
611 Consequently, the proposed combined retrieval represents a highly valuable architectural upgrade for monitoring severe
612 weather in complex coastal environments like the Eastern Mediterranean. However, it must be acknowledged that there are
613 many sites worldwide where the deployment of microwave radiometers may not be justified. Given the high capital and
614 operational costs of radiometric hardware, the presence of other unmitigated geodetic uncertainties, and the adequate
615 performance of static T_m models in less thermodynamically complex regions, this synergistic approach is best reserved for
616 targeted deployments in highly vulnerable climatic hotspots.

617 For the climate-sensitive Eastern Mediterranean region, relying on static models for GNSS processing risks systematically
618 masking moisture trends during heatwaves and deep convection. We therefore recommend the operational integration of
619 collocated MWR observations into national GNSS processing chains. Where collocation is not feasible, future work should
620 focus on assimilating MWR-derived diurnal shape functions into static models to bridge the gap between climatology and
621 reality. This study establishes the "Corrected Synergistic Method" as a robust benchmark for generation of climate-quality
622 water vapour datasets in complex thermodynamic environments. From an operational perspective, relying exclusively on
623 MWRs for regional moisture monitoring is constrained by high capital costs, maintenance complexity, and signal degradation
624 during precipitation events. Conversely, GNSS networks provide highly cost-effective, dense, and all-weather monitoring

625 capabilities. The primary operational interest of this proposed methodology is the 'supersite' calibration strategy: utilizing a
626 centralized MWR to capture the true, real-time thermodynamic diurnal variations that static models like HGPT2 miss, and
627 subsequently assimilating these dynamic T_m corrections over a much wider, regional network of standard GNSS receivers.
628 This synergy allows forecasting centers to leverage the superior thermodynamic accuracy of a single MWR to drastically
629 improve the high-resolution, continuous PWV datasets generated by dense, low-cost GNSS infrastructure.

630

631 **Code and data availability**

632 The GNSS Zenith Total Delay estimates, the Microwave Radiometer (MWR) brightness temperatures, and the retrieved
633 profiles collected under the CYGMEN project, along with the custom processing scripts used for the linear bias correction, are
634 available by contacting Dr. Christina Oikonomou (CYGMEN Project Coordinator). The high-resolution radiosonde profiles
635 provided by the Department of Meteorology (DoM), Cyprus, are under restricted access due to third-party data policies and
636 can be requested by contacting the department through their official website. The Tefnut PP software used for GNSS processing
637 is available at <https://gnutsoftware.com/software/tefnut>. The ERA5 reanalysis data can be obtained from the Copernicus
638 Climate Change Service (C3S) Climate Data Store at <https://doi.org/10.24381/cds.bd0915c6> (Hersbach et al., 2020).

639 **Author contributions**

640 ANP carried out the GNSS, MWR, and Radiosonde data processing, performed the synergistic PWV retrievals and error
641 diagnosis, and wrote the initial version of the paper. CO and HH conceptualized the study, acquired the funding and resources
642 for the CYGMEN infrastructure, and supervised the investigation. All authors discussed the results, edited, and proofread the
643 paper.

644

645 **Competing interests**

646 All authors declare that they have no conflict of interest.

647

648 **Acknowledgements**

649 We would like to express our sincere gratitude to the Cyprus Department of Meteorology (DoM) and in particular to Physicist
650 and Meteorology Officer Dr. Demetris Charalambous, for his invaluable guidance and for providing access to essential
651 resources at Athalassa observatory in Nicosia, Cyprus.

652

653 **Financial support**

654 The present study is funded by the Strategic Infrastructure project CYGMEN, which is implemented in the frames of Cohesion
655 Policy Programme “THALIA 2021-2027” and is co-funded by the European Union.
656

657 **References**

658 Askne, J. and Nordius, H.: Estimation of tropospheric delay for microwaves from surface weather data, *Radio Sci.*, 22, 379–
659 386, <https://doi.org/10.1029/RS0221003p00379>, 1987.

660 Bennartz, R. and Bauer, P.: Sensitivity of microwave radiances at 85–183 GHz to precipitating ice particles, *Radio Sci.*, 38,
661 8075, <https://doi.org/10.1029/2002RS002626>, 2003.

662 Bennett, G. V. and Jupp, A.: Operational assimilation of GPS zenith total delay observations into the Met Office numerical
663 weather prediction models, *Mon. Weather Rev.*, 140, 2706–2719, <https://doi.org/10.1175/MWR-D-11-00156.1>, 2012.

664 Bevis, M., Businger, S., Herring, T. A., Rocken, C., Anthes, R. A., and Ware, R. H.: GPS meteorology: Remote sensing of
665 atmospheric water vapor using the Global Positioning System, *J. Geophys. Res.*, 97, 15787–15801,
666 <https://doi.org/10.1029/92JD01517>, 1992.

667 Bevis, M., Businger, S., Chiswell, S., Herring, T. A., Anthes, R. A., Rocken, C., and Ware, R. H.: GPS meteorology: Mapping
668 zenith wet delays onto precipitable water, *J. Appl. Meteorol.*, 33, 379–386, [https://doi.org/10.1175/1520-0450\(1994\)033<0379:GMMZWD>2.0.CO;2](https://doi.org/10.1175/1520-0450(1994)033<0379:GMMZWD>2.0.CO;2), 1994.

670 Böhm, J., Möller, G., Schindelegger, M., Pain, G., and Weber, R.: Development of an improved empirical model for slant
671 delays in the troposphere (GPT2w), *GPS Solut.*, 19, 433–441, <https://doi.org/10.1007/s10291-014-0403-7>, 2015.

672 Bolton, D.: The computation of equivalent potential temperature, *Mon. Weather Rev.*, 108, 1046–1053,
673 [https://doi.org/10.1175/1520-0493\(1980\)108<1046:TCOEPT>2.0.CO;2](https://doi.org/10.1175/1520-0493(1980)108<1046:TCOEPT>2.0.CO;2) 1980.

674 Brenot, H., Neméghaire, J., Delobbe, L., Clerbaux, N., De Meutter, P., Deckmyn, A., Delcloo, A., Frappez, L., and Van
675 Roozendael, M.: Preliminary signs of the initiation of deep convection by GNSS, *Atmos. Chem. Phys.*, 13, 5425–5449,
676 <https://doi.org/10.5194/acp-13-5425-2013>, 2013.

677 Bock, O., Bossler, P., Flamant, C., Doerflinger, E., Jansen, F., Fages, R., Bony, S. and Schnitt, S.: Integrated water vapour
678 observations in the Caribbean arc from a network of ground-based GNSS receivers during EUREC 4 A. *Earth System Science*
679 *Data*, 13(5), pp.2407-2436. <https://doi.org/10.5194/essd-13-2407-2021>. 2021.

680 Cimini, D., Westwater, E. R., Gasiewski, A. J., Klein, M., Leuski, V. Y., and Dowlatshahi, S.: Thermodynamic atmospheric
681 profiling during the 2010 Winter Olympics using ground-based microwave radiometry, *IEEE T. Geosci. Remote*, 49, 4959–
682 4969, <https://doi.org/10.1109/TGRS.2011.2154337>, 2011.

683 Cimini, Domenico, Tim J. Hewison, Lorenz Martin, Jürgen Güldner, Catherine Gaffard, and Frank S. Marzano. "Temperature
684 and humidity profile retrievals from ground-based microwave radiometers during TUC." *Meteorologische Zeitschrift* 15, no.
685 1: 45-56. 2006.

686 Crewell, S. and Löhnert, U.: Accuracy of boundary layer temperature profiles retrieved with multifrequency multiangle
687 microwave radiometry, *IEEE T. Geosci. Remote*, 45, 2195–2201, doi: 10.1109/TGRS.2006.888434. 2007.

688 Douša, J. and Václavovic, P.: Real-time zenith tropospheric delays in support of numerical weather prediction applications,
689 *Adv. Space Res.*, 53, 1347–1358, <https://doi.org/10.1016/j.asr.2014.02.021>, 2014.

690 Davis, J. L., Herring, T. A., Shapiro, I. I., Rogers, A. E. E., and Elgered, G.: Geodesy by radio interferometry: Effects of
691 atmospheric modeling errors on estimates of baseline length, *Radio Sci.*, 20, 1593–1607,
692 <https://doi.org/10.1029/RS020i006p01593>, 1985.

693 Foth, A., Lochmann, M., Saavedra Garfias, P. and Kalesse-Los, H.: Determination of low-level temperature profiles from
694 microwave radiometer observations during rain. *Atmospheric Measurement Techniques*, 17(24), pp.7169-7181, 2024.

695 Gaffen, D. J.: Temporal inhomogeneities in radiosonde temperature records, *J. Geophys. Res.*, 99, 3667–3676,
696 <https://doi.org/10.1029/93JD03179>, 1994.

697 Giannadaki, D., Oikonomou, C., Haralambous, H., Tymvios, F., and Loizou, E.: Validation of precipitable water vapour
698 products using CyMETEO GNSS network in Cyprus, in: Eleventh International Conference on Remote Sensing and
699 Geoinformation of the Environment (RSCy2025), Vol. 13816, 397–409, SPIE, 2025.

700 Giorgi, F.: Climate change hot-spots, *Geophys. Res. Lett.*, 33, L08707, <https://doi.org/10.1029/2006GL025734>, 2006

701 Guerova, G., Jones, J., Douša, J., Dick, G., de Haan, S., Pottiaux, E., Bock, O., Pacione, R., Elgered, G., Vedel, H., and Bender,
702 M.: Review of the state of the art and future prospects of the ground-based GNSS meteorology in Europe, *Atmos. Meas. Tech.*,
703 9, 5385–5406, <https://doi.org/10.5194/amt-9-5385-2016>, 2016.

704 Held, I. M. and Soden, B. J.: Robust responses of the hydrological cycle to global warming, *J. Climate*, 19, 5686–5699,
705 <https://doi.org/10.1175/JCLI3990.1>, 2006.

- 706 Healy, S.B.: Refractivity coefficients used in the assimilation of GPS radio occultation measurements. *Journal of Geophysical*
707 *Research: Atmospheres*, 116(D1). <https://doi.org/10.1029/2010JD014013>. 2011.
- 708 Jiang, P., Ye, S., Chen, D., Liu, Y., and Xia, P.: Development of time-varying global gridded Ts-Tm model for precise GPS-
709 PWV retrieval, *Atmos. Meas. Tech.*, 12, 1233–1249, <https://doi.org/10.5194/amt-12-1233-2019>, 2019.
- 710 Jones, J., Guerova, G., Douša, J., Dick, G., de Haan, S., Pottiaux, E., Bock, O., Pacione, R., Elgered, G., Vedel, H., and Bender,
711 M.: Advanced GNSS Tropospheric Products for Monitoring Severe Weather Events and Climate, Springer, Cham,
712 <https://doi.org/10.1007/978-3-030-13901-8>, 2020.
- 713 Kiehl, J. T. and Trenberth, K. E.: Earth's annual global mean energy budget, *B. Am. Meteorol. Soc.*, 78, 197–208,
714 [https://doi.org/10.1175/1520-0477\(1997\)078<0197:EAGMEB>2.0.CO;2](https://doi.org/10.1175/1520-0477(1997)078<0197:EAGMEB>2.0.CO;2), 1997.
- 715 Lan, Z., Zhang, B., and Geng, T.: Establishment and analysis of global gridded Tm-Ts relationship model, *Geodesy and*
716 *Geodynamics*, 7, 101–107, <https://doi.org/10.1016/j.geog.2016.02.001>, 2016.
- 717 Lelieveld, J., Hadjinicolaou, P., Kostopoulou, E., Chenoweth, J., El Maayar, M., Giannakopoulos, C., Hannides, C., Lange,
718 M. A., Tanarhte, M., Tyrllis, E., and Xoplaki, E.: Climate change and impacts in the Eastern Mediterranean and the Middle
719 East, *Climatic Change*, 114, 667–687, <https://doi.org/10.1007/s10584-012-0418-4>, 2012.
- 720 Li, H., Wang, X., Wu, S., Zhang, K., Chen, X., Qiu, C., Zhang, Q., and Li, L.: Development of an improved model for
721 prediction of short-term heavy precipitation based on GNSS-derived PWV, *Remote Sens.*, 12, 4101,
722 <https://doi.org/10.3390/rs12244101>, 2020.
- 723 Löhnert, U. and Maier, O.: Operational profiling of temperature using ground-based microwave radiometry at Payerne:
724 Prospects and challenges, *Atmos. Meas. Tech.*, 5, 1121–1134, <https://doi.org/10.5194/amt-5-1121-2012>, 2012.
- 725 Mateus, P., Mendes, V. B., and Plecha, S. M.: HGPT2: an ERA5-based global model to estimate relative humidity, *Remote*
726 *Sens.*, 13, 2179, <https://doi.org/10.3390/rs13112179>, 2021.
- 727 Ning, T. and Elgered, G.: Intercomparison of MAX-DOAS vertical profile retrieval algorithms: studies on field data from the
728 CINDI-2 campaign, *Atmos. Meas. Tech.*, 14, 1–35, <https://doi.org/10.5194/amt-14-1-2021>, 2021.
- 729 Ning, Tong, J. Wang, G. Elgered, G. Dick, J. Wickert, Markus Bradke, M. Sommer, R. Querel, and D. Smale. "The uncertainty
730 of the atmospheric integrated water vapour estimated from GNSS observations." *Atmospheric Measurement Techniques* 9, no.
731 1. 79-92. doi:10.5194/amt-9-79-2016. 2016.

732 Pakkattil, A., Parde, A. N., Wagh, S., Lonkar, P., and Ghude, S. D.: Wintertime Intercomparison of Specific Humidity and
733 Temperature Profiles Measured by Microwave Radiometer (MWR), Radiosonde, and INSAT-3DR Sounder Over Delhi, India,
734 *J. Geophys. Res. Atmos.*, 130, e2025JD044462, <https://doi.org/10.1029/2025JD044462>, 2025.

735 Parde, A. N., Ghude, S. D., Prasad, V. S., Hari Prasad, K. B. R. R., Dhargar, N. G., Lonkar, P., and Rajeevan, M.: Influence
736 of ground-based microwave radiometer profile assimilation on fog genesis forecasts in the winter boundary layer of Northern
737 India, *J. Geophys. Res. Atmos.*, 130, e2024JD042224, <https://doi.org/10.1029/2024JD042224>, 2025.

738 Oikonomou, C., Tymvios, F., Pikridas, C., Bitharis, S., Balidakis, K., Michaelides, S., ... and Charalambous, D.: Tropospheric
739 delay performance for GNSS integrated water vapor estimation by using GPT2w model, ECMWF's IFS operational model and
740 in situ meteorological data, *Adv. Geosci.*, 45, 363–375, <https://doi.org/10.5194/adgeo-45-363-2018>, 2018.

741 Realini, E., Gatti, A., Reguzzoni, M., Sampietro, D., and Venuti, G.: GNSS-based precipitable water vapor retrieval for severe
742 weather monitoring: The 2014 Genoa flood case study, *Adv. Space Res.*, 53, 1–10, <https://doi.org/10.1016/j.asr.2014.02.015>,
743 2014.

744 Rüeger, J. M.: Refractive index formulae for radio waves, in: Proceedings of the FIG XXII International Congress,
745 Washington, D.C., USA, 19–26 April 2002, 1–13, 2002.

746 Ross, R. J. and Elliott, W. P.: Tropospheric water vapor climatology and trends over North America: 1973–93, *J. Climate*, 9,
747 3561–3574, [https://doi.org/10.1175/1520-0442\(1996\)009<3561:TWVCAT>2.0.CO;2](https://doi.org/10.1175/1520-0442(1996)009<3561:TWVCAT>2.0.CO;2). 1996.

748 Saastamoinen, J.: Atmospheric correction for the troposphere and stratosphere in radio ranging satellites, in: The Use of
749 Artificial Satellites for Geodesy, *Geophys. Monogr. Ser.*, 15, 247–251, AGU, Washington, D.C.,
750 <https://doi.org/10.1029/GM015p0247>, 1972.

751 Soden, B. J. and Lanzante, J. R.: An assessment of satellite and radiosonde climatologies of upper-tropospheric water vapor,
752 *J. Climate*, 9, 1235–1250, [https://doi.org/10.1175/1520-0442\(1996\)009<1235:AAOSAR>2.0.CO;2](https://doi.org/10.1175/1520-0442(1996)009<1235:AAOSAR>2.0.CO;2), 1996.

753 Steinke, S., Ebell, K., Löhnert, U., Bozzo, A., Crewell, S., and Turner, D. D.: Assessment of small-scale integrated water
754 vapour variability during HOPE, *Atmos. Chem. Phys.*, 15, 2675–2692, <https://doi.org/10.5194/acp-15-2675-2015>, 2015.

755 Thayer, G. D.: An improved equation for the radio refractive index of air, *Radio Sci.*, 9, 803–807,
756 <https://doi.org/10.1029/RS009i010p00803>, 1974.

757 Trenberth, K. E., Fasullo, J., and Smith, L.: Trends and variability in column-integrated atmospheric water vapor, *Clim.*
758 *Dynam.*, 24, 741–758, <https://doi.org/10.1007/s00382-005-0017-4>, 2005.

759 Van Malderen, R., Brenot, H., Pottiaux, E., Beirle, S., Hermans, C., De Mazière, M., ... and Bruyninx, C.: A multi-site
760 intercomparison of integrated water vapour observations for climate change analysis, *Atmos. Meas. Tech.*, 7, 2487–2512,
761 <https://doi.org/10.5194/amt-7-2487-2014>, 2014.

762 Van Malderen, R., Pottiaux, E., Stankunavicius, G., Beirle, S., Wagner, T., Brenot, H., Bruyninx, C. and Jones, J.: Global
763 spatiotemporal variability of integrated water vapor derived from GPS, GOME/SCIAMACHY and ERA-Interim: Annual
764 cycle, frequency distribution and linear trends. *Remote Sensing*, 14(4), p.1050, <https://doi.org/10.3390/rs14041050>, 2022.

765 Van Baelen, J., Aubagnac, J.P. and Dabas, A.: Comparison of near–real time estimates of integrated water vapor derived with
766 GPS, radiosondes, and microwave radiometer. *Journal of Atmospheric and Oceanic Technology*, 22(2), pp.201-210, 2005.

767 Vaquero-Martínez, J., Antón, M., Ortiz de Galisteo, J. P., Cachorro, V. E., Wang, H., González-Abad, G., ... and Costa, M. J.:
768 Inter-comparison of integrated water vapor from ground-based GPS and satellite remote sensing at Mediterranean sites, *IEEE*
769 *J. Sel. Top. Appl.*, 11, 1718–1728, <https://doi.org/10.1109/JSTARS.2018.2812804>, 2018.

770 Ware, R., Cimini, D., Herzegh, P., Marzano, F., Vivekanandan, J. and Westwater, E.: Ground-based microwave radiometer
771 measurements during precipitation. In *8th Specialist Meeting on Microwave Radiometry* (pp. 24-27), 2004.

772 Wang, Junhong, Liangying Zhang, and Aiguo Dai. "Global estimates of water-vapor-weighted mean temperature of the
773 atmosphere for GPS applications." *Journal of Geophysical Research: Atmospheres* 110, no. D21. doi:10.1029/2005JD006215.
774 2005.

775 Yao, Y., Zhang, B., Yue, S., Xu, C., and Peng, W.: Analysis of the global Tm-Ts correlation and establishment of the latitude-
776 related linear model, *Chin. Sci. Bull.*, 59, 2340–2347, <https://doi.org/10.1007/s11434-014-0275-9>, 2014.

777 Ziskin Ziv, S., Yair, Y., Alpert, P., Uzan, L., and Reuveni, Y.: The diurnal variability of precipitable water vapor derived from
778 GPS tropospheric path delays over the Eastern Mediterranean, *Atmos. Res.*, 249, 105307,
779 <https://doi.org/10.1016/j.atmosres.2020.105307>, 2021.

780 Ziskin Ziv, S., Alpert, P., and Reuveni, Y.: Long-term variability and trends of precipitable water vapour derived from GPS
781 tropospheric path delays over the Eastern Mediterranean, *Int. J. Climatol.*, 41, 6433–6454, <https://doi.org/10.1002/joc.7205>,
782 2021.

783 Zittis, G., Hadjinicolaou, P., Klangidou, M., et al.: A multi-model, multi-scenario, and multi-domain analysis of regional
784 climate projections for the Mediterranean, *Reg. Environ. Change*, 19, 2621–2635, [https://doi.org/10.1007/s10113-019-01565-](https://doi.org/10.1007/s10113-019-01565-w)
785 [w](https://doi.org/10.1007/s10113-019-01565-w), 2019.